Eur. Phys. J. B **55**, 297–322 (2007)
DOI: 10.1140/epjb/e2007-00057-y

THE EUROPEAN PHYSICAL JOURNAL B

Dynamics of a circular array of liquid columns

Dynamics of an array of liquid columns

P. Brunet[1,2,a], J.-M. Flesselles[2], and L. Limat[1,3]

[1] Laboratoire de Physique et Mécanique des Milieux Hétérogènes (PMMH) UMR 7636 of CNRS, ESPCI, 10 rue Vauquelin 75005 Paris, France
[2] Saint-Gobain Recherche, 39 quai Lucien Lefranc. 93303 Aubervilliers Cedex, France
[3] Laboratoire Matière et Systèmes Complexes, UMR of CNRS, University Paris 7, 2 Place Jussieu 75005 Paris, France

Received 5 July 2006 / Received in final form 7 February 2007
Published online 2 March 2007 –

Abstract. We report on an experimental study of an array of liquid columns, hanging below an overflowing circular dish fed at a constant flow-rate. This one-dimensional pattern exhibits spatio-temporal chaos as well as a host of ordered dynamical regimes, depending on flow-rate, initial positions, number of columns, and liquid properties. In this paper, we present stability diagrams obtained with liquids of different properties and an extensive quantitative study of the ordered, predictable dynamical states. Some destabilization mechanisms of these regimes are also presented.

PACS. 05.45.-a Nonlinear dynamics and chaos – 47.20.Lz Secondary instabilities – 47.20.Ma Interfacial instabilities (e.g., Rayleigh-Taylor)

1 Introduction

Pattern-forming instabilities are known to exhibit rich and fascinating dynamical behavior [1,2]. They are observed in every day life in various forms such as arrays of clouds, ripples in underwater sand sheared by the tide, or snow flakes. They have been studied intensively in the last decades because some of their properties are associated to the generic concepts of symmetry-losses and transition toward disorder. They are also known to present analogies with transition scenarios toward fluid turbulence. For example, recently a set of oblique or traveling waves have been evidenced in plane Couette flow [3,4] and in Poiseuille flow [5]. The destabilization of a primary flow via the emergence of a pattern of static or traveling waves is seemingly a generic feature in many non-linear systems.

As a sub-class of these systems, one-dimensional destabilizing fronts have focused interest because of their relative simplicity. Directional viscous fingering (also mentioned as the printer's instability) [6–11], directional solidification [12–15], arrays of ferrofluid pikes in an oscillating magnetic field [16] or a thin layer of liquid in a thermal gradient [17] are examples of such one-dimensional fronts. The damped Kuramoto-Sivashinsky (KS) equation [18–21] exhibits striking analogies with these systems and is presumably the simplest numerical equivalent available.

The 'circular fountain' presented here and previously studied in [22–26], provides another example of such a destabilizing interfacial front. It consists in an overflowing circular dish below which an array of liquid columns forms (see Fig. 1a). Basically, this pattern can be seen as the result of a combination between the Rayleigh-Taylor instability [27–29] of a thin layer hanging below a solid substrate, and a permanent supply of liquid with the flow-rate Q. Incidentally, this liquid supply counterbalances the Rayleigh-Plateau instability of each column [27], which would cause the columns to pinch-off at low flow-rate and would turn them into dripping sites. Pioneering studies on arrays of columns formed below a horizontal cylinder or at the lowest edge of an inclined plane were worked out by Carlomagno [30] and by Pritchard [31]. The latter already remarked that such a network exhibited unstable and complex dynamics. Afterwards, Giorgiutti et al. [32–34] used this system as a benchmark for capturing and studying the dynamics of destabilizing interfacial fronts. The geometry of the circular dish appeared then as the most suitable one [22,23,33,34]: it avoids any edge effects that can lead to unwanted perturbations or can bias the long time behavior of columns. In particular in our system, domains of drifting columns can propagate endlessly, just like in an infinite medium [22,24].

[a] *Present address*: Department of Mathematics, University of Bristol, BS81TW Bristol, UK;
e-mail: p.brunet@bristol.ac.uk

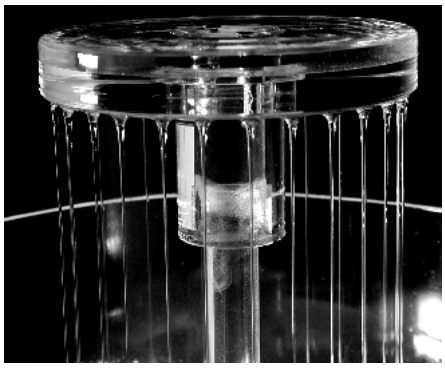

(a)

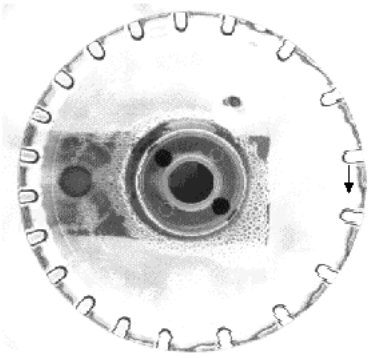

(b)

Fig. 1. The circular fountain experiment. (a) Side view of the array of liquid columns (dish diameter $d = 10$ cm, silicon oil $\eta = 100$ cP). (b) The array viewed from above, suitable to extract grey levels and build spatiotemporal diagrams.

In such pattern-forming systems, the direct resolution of equations is far from obvious, and generally tells little about the non-linear dynamics of interest. Most often, only the first stages of the primary instability can be solved. This is the reason why these systems have been described with phenomenological models, that involve local or global symmetry breaking from a basic reference state, generally, a static spatially-periodic pattern: see [35–41] amongst many other studies, and [1] for an exhaustive review. The determination of relevant parameters in these models needs inputs from experiments, particularly in the further stages, far beyond secondary instability thresholds [40,41].

The circular fountain is first of all a curiosity of the hydrodynamics, as illustrated in the global drifting pattern — a remarkable liquid merry-go-round. It also exhibits a rich dynamics that recovers most of the phenomenology of pattern-forming interfaces, which can be compared to other systems [6–21] although it involves really different physical mechanisms.

The scope of this paper is to present an exhaustive study of different dynamical regimes when both the flow-rate and the physical properties of the liquid (mainly its viscosity here) are varied. In particular, we present stability diagrams assembling the limits of different possible states in the parameters space. We show extensive measurements of these dynamical regimes as well as their different break-up scenarios.

In our experiment, the natural control parameter is the flow-rate per unit length Γ, which is equal to the volumetric flow-rate divided by the perimeter of the circle along which columns travel,

$$\Gamma = \frac{Q}{\pi d} \tag{1}$$

with silicon oil (characteristics are given later), Γ is roughly between 0.05 and 0.7 cm^2/s for a columns pattern. Static columns are about 1 cm apart, but the spacing can get up to 2.2 cm between two drifting columns. Figure 1b offers a view from above, with a zone of dilation at the upper right side of the picture, related to a local drift suggested by an arrow.

The selected state is not only determined by Γ, but also by a set of initial conditions, like in most of out-of-equilibrium systems. These initial conditions can easily be tuned by the experimentalist [22,24,25], and it is one of the advantages of this system: with one or several needles, put in contact with the top of the columns, it is possible to set their initial position and initial motion. Viscosity η is also a crucial parameter. The number of the different available states and the complexity of the dynamics increase with viscosity. In particular, if it is greater than 90 cP, a regime of spatio-temporal disorder can be observed. No such regime could be observed in the first studies carried out at lower viscosities [22,23]. The chaotic states have been studied in details in [26] and compared to disordered behavior in other systems [6,15–17,42,43]. They usually involve the generic scenario of spatiotemporal intermittency (STI), i.e. a coexistence of laminar domains and turbulent patches. Chaotic regimes in the pattern of columns, and presumably in other destabilizing fronts, are somehow different as they involve spatiotemporal singularities in the phase space, called 'defects' (i.e. births and coalescence of Cols. [26]). These defects result from complex interactions between laminar domains, particularly propagative structures and oscillating patches [26]. In most situations, they are clearly the signature of the break-up of states that have been driven out of their domain of stability.

Let us finally mention a two-dimensional extension of this system [44,45], where the network of columns is self-organized around a hexagonal structure. Local departures from this basic hexagonal state lead to dynamical states, such as localized oscillations or a pair of columns, propagative solitons or oscillating arrays of columns. A quantitative study of turbulent states in 2D has been carried out in [46].

The paper is organized as follows: after a short review of models of cellular structure dynamics (Sect. 2), we describe the experimental set-up (Sect. 3). Section 4 offers a general overview of the dynamics of the pattern of liquid columns. Measurements related to different states are reported in Section 5. Section 6 is dedicated to different break-up scenarios of several regimes. Section 7 concludes the paper.

2 A few notions on existing models for 1D cellular patterns

2.1 Describing a cellular pattern with a symmetry-based model: the example of parity-breaking drifting cells

Even if the direct resolution of the complete set of equations has led to remarkable achievements in some pattern-forming instabilities, these studies are mostly restricted to the very first stages of the primary instability. Their extension to secondary instabilities would constitute a heavy mathematical work, which furthermore would not bring out the general characteristics one wishes to emphasize. Instead, it is common to reduce the problem to a more phenomenological approach, by seeking for simpler models, although rich enough to exhibit the complex behaviors one expects. The framework of coupled equations linking spatial phase and amplitude of a secondary bifurcated solution, related to considerations of possible broken symmetries in the system, constitutes a general and mathematically tractable approach.

For one-dimensional stationary patterns, Coullet and Iooss have listed all possible secondary bifurcations towards dynamical states from symmetry arguments [35]. In this approach, the pattern is represented by a one-dimensional function $U(x,t)$, of one space variable x and of time t, that obeys simple general laws. The function $U(x,t)$ is generally the sum of a spatially periodic function $U_0(x+\phi)$ chosen as a reference, and another function $u(x+\phi,t)$ which is a combination of different modes. The quantity ϕ is the spatial phase of the pattern.

$$U(x,t) = U_0(x+\phi) + u(x+\phi,t) \quad (2)$$

$$u(x+\phi,t) = \sum A_\alpha(x+\phi_\alpha,t)\, m_\alpha(x+\phi_\alpha,t) \quad (3)$$

α is the index of unstable modes m_α that can be time-dependent or not. A_α are the amplitude of these modes. It has been shown that ten generic modes exist, corresponding to ten different broken symmetries. Figure 2 illustrates how such a function can represent a pattern of cells, in specific states.

For example, the well-known propagating domains of drifting cells [8,10,12,14,15,22–25,36] are associated to a left-right symmetry breaking. Figure 2 (bottom sketch) gives kinetic and geometrical definitions related to this state: λ_0 (resp. λ_1) stands for the wavelength selected outside (resp. inside) a propagative domain; V_d stands for the drift velocity of cells (phase speed) and V_g for the wall velocity of the domain (group velocity). The mode $m_\alpha(x+\phi_\alpha,t)$ is an anti-symmetrical function of x, that is added to the reference U_0 in the bulk of a domain [36]. The amplitude of the mode A_α and the phase ϕ_α are supposed to vary slowly with space and time variables. From symmetry arguments, one can deduce coupled partial differential equations for A_α and ϕ_α. When one only gets restricted to this specific antisymmetric mode — the assumption is valid inside a propagating domain — the following equations are found [36]:

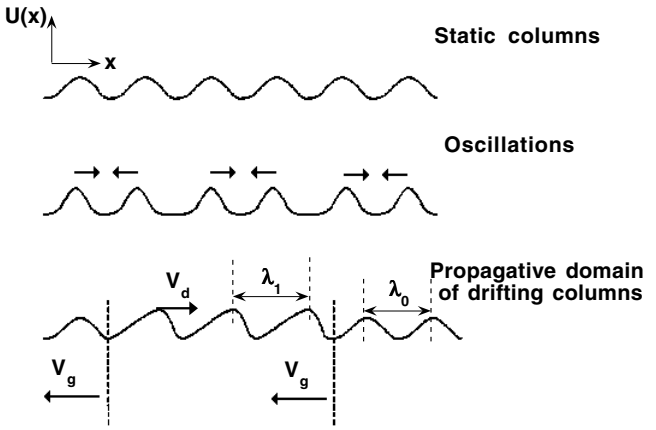

Fig. 2. Sketch of typical one-dimensional cellular pattern dynamics defined by a function $U(x,t)$ (Eq. (3)). From top to bottom, a periodic function represents static states; a time-dependent period-doubled function represents out-of-phase oscillations; a superimposition of an antisymmetric mode and a symmetric one (in regards to the left-right reflection) represents a propagative domain of broken-parity drifting cells.

$$A_t = (\mu + \epsilon\phi_x)A + DA_{xx} + \gamma AA_x - \delta A^3 + \dots \quad (4)$$

$$\phi_t = \zeta A + D_\phi \phi_{xx} + \dots \quad (5)$$

These equations have been restricted to their lowest orders for the powers of A and ϕ and their mutual combinations. This assumes that the system lies sufficiently close to the bifurcation threshold, so that amplitudes keep small. Generally, μ appears as the natural control parameter of the system. It some sense, the coupling $\epsilon\phi_x$ means that the threshold of the bifurcation also depends on the phase gradient. In this minimal model also, the coefficients δ and ζ are *a priori* independent on the phase gradient ϕ_x.

The quantity ϕ_x is also the difference between the local wavenumber and the reference wavenumber k_0:

$$\phi_x = k_1 - k_0 = 2\pi\left(\frac{1}{\lambda_1} - \frac{1}{\lambda_0}\right). \quad (6)$$

The time derivative of the phase ϕ_t is related to the drift velocity of the cell, by the following relationship:

$$\phi_t = V_d k_1. \quad (7)$$

Assuming that the phase gradient and the asymmetry A are constant inside a propagative domain — which is equivalent to say that all the drifting cells are identical and at equal distance to their nearest neighbors, all the space derivatives of A and ϕ_x can be removed from (4) and (5). Thus, it is found that A and ϕ_t are proportional: $\phi_t = \zeta A$. The solution for A at equilibrium ($A_t = 0$) is:

$$A^2 = (\mu + \epsilon\phi_x)/\delta. \quad (8)$$

Thus, the quantity to be measured is $(V_d k_1)^2$, that is predicted to vary linearly with the quantity $(\mu + \epsilon\phi_x)$. In

the printer's instability experiments, the drift velocity was found to vary as the square-root of the speed of the internal cylinder v_i [8,10,11] and then the identification of μ with v_i was obvious. It was even possible to directly measure A from the shape of the interface [11]. In directional solidification μ was identified to a combination of the wavelength λ and of the pulling velocity that reads: λV^2. In the pattern of columns, the identification of μ to the flow-rate Γ was also straightforward from measurements. From (6) and (8), one obtains:

$$(V_d k_1)^2 = \frac{\zeta^2}{\delta}(\Gamma + \epsilon(k_1 - k_0)). \quad (9)$$

Combined with a control of the wavelength, this relation has been used in reference [24] to determine the coefficients ϵ, ζ and δ for the array of liquid columns. Surprisingly, this study revealed that ζ and δ are in fact ϕ_x dependent, which means that additional non-linearities of the kind $A^3\phi_x$ and $A\phi_x$ respectively in equations (4) and (5) must also be considered. Another unexpected feature was also that this model, once generalized, was still valid far from threshold of the secondary bifurcation [24], even though it was built under the assumptions of close-to-threshold conditions. More details will be presented in Section 5.

Let us mention another model, based on nonlinear interactions between the basic mode k_0 and its first spatial harmonic $2k_0$ (often called '$k - 2k$ model') described for instance in [37]. This model predicts a broken parity of the cells, leading to their drift, if there exists a phase mismatch between the basic mode and its first harmonic. This model is particularly attractive for interfacial fronts, where careful observations of the interface reveal the following fact: the shape of moving cells is the superimposition of primary cells and of smaller secondary cells that tend to grow between the primary ones (see e.g. [10,11]). This is related to a insufficiently damped spatial harmonic. Its relevance has also been emphasized in the KS equation [21].

2.2 Possible extension of these models far from threshold

One of the remaining issues in these systems is to what extent the different patterns can be compared to each other, when one examines their specific behavior far from threshold. The model by Coullet and Iooss [35] offers a framework for secondary instabilities close to their own threshold. However, this model is not adapted to predict certain far-from-threshold behavior. An extension of this model has recently been built by Gil [40]. It introduces a possible phase mismatch between the primary and the secondary mode as a new variable, and allows discontinuities in the amplitude and phase of the modes. This model has provided promising results, comparable to those obtained in numerical and experimental systems that are driven far from secondary thresholds, such as (A) oscillating wakes at the trailing edge of localized propagative domains, (B) phase mismatch and amplitude holes in extended oscillating regimes and (C) turbulent oscillating patches seemingly associated to STI. Situation (A) is observed in the printer's instability [7], in directional solidification [14] and the pattern of columns [25], although with specific relationships between the propagation speed and the pulsation of oscillations that does not seem to be reproduced by the model. Situation (B) has been observed in directional solidification [15] as well as in the array of columns [48] (see also later in this paper). Situation (C) is more likely to be related to STI in the Rayleigh-Bénard convection [42], where turbulent patches are characterized by existence of cells that become blur and loose their initial shape. Spatio-temporal complexity appears differently in our system, as columns still keep the same shape they have in laminar states. The complexity only lies in the motions of the columns and not in the fluctuations of their own shapes. The complex motions are sustained by multiple interactions between propagative and oscillating inclusions that give rise to defects, i.e. singularities in the space phase variable. To our knowledge, such a behavior has not been seen in Gil's model, but has been reproduced in the Ginzburg-Landau equation (CGLE) [47] and KS equations [21].

All these models, dedicated to pattern-forming instabilities [21,47,49–51], include a large number of tunable parameters, which are not easy to relate to physical quantities. In order to capture the minimal set of required parameters, one needs some inputs from experiments. In the following, we describe the specific behavior of the pattern of columns and systematically try to compare to other experiments and numerical models when possible.

3 Experimental set-up

Silicon oil of viscosity η, surface tension σ and density ρ at 20 °C is injected at the center of the dish e through a hollow vertical tube, see Figure 1a. The properties of these liquids are listed on Table 1. The flow is measured with a float flow-meter d (Brooks Full View GT 1024). It is set by a gear pump a (Ismatec BVP Z) followed by a cylindrical half-filled chamber c, that damps residual pulsations (radius = 20 cm, height = 15 cm). The imposed flow-rate Q ranges from 2 to 30 cm^3/s. The oil temperature is regulated with a thermal bath b at 20 °C with an accuracy of one degree. Plexiglas circular dishes with different external diameter (d) have been used. The flow-rate per unit length Γ is determined with an accuracy of ± 0.005 cm^2/s. Reported data are obtained with two dishes of diameter $d = 10$ cm and 16.7 cm. The dish horizontality is crucial to obtain reproducible measurements. It is accurately tuned with a three-feet table supporting the setup, by simply checking the uniformity of amplitudes of oscillating columns when the system undergoes a transition to an oscillatory state, as described in more details elsewhere [24].

The pattern of columns is observed from above by a CCD video camera, and lightened by a circular neon tube put in the periphery of the dish and slightly below it. Columns appear as series of U-shaped spots (see Fig. 1b).

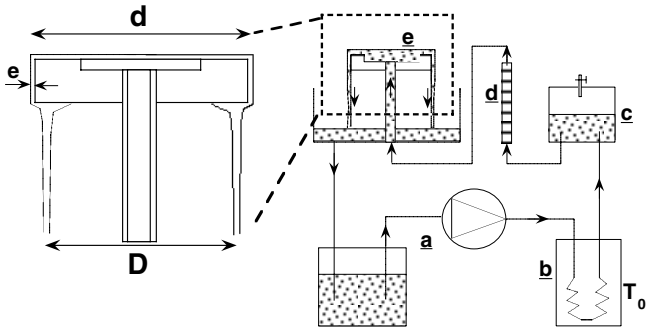

Fig. 3. Experimental setup. See text for details.

Table 1. Physical properties of the liquids.

Oil	η (cP)	ρ (g/cm^3)	γ (dyn/cm)
PDMS 47V20	20	0.95	20.6
PDMS 47V50	50	0.96	20.7
PDMS 47V100	100	0.97	20.7
PDMS 47V200	200	0.97	20.7

Spatio-temporal diagrams are built by recording grey levels along the circle which intercepts the columns' center. Experimentally, the diameter of this circle was found to be independent on the flow-rate [23,24] and respectively equal to $D = 9.54$ cm and $D = 16.20$ cm for the dishes of diameter $d = 10.00$ cm and $d = 16.70$ cm. Images were digitized using *NIH Image 1.62* on a Macintosh computer. To achieve reliable image processing, it is of first importance that the background color of pictures acquired from above be as homogeneous as possible and that the edge of columns be visibly sharp, in order to have easy-to-analyze diagrams. Black paper covers the surround between the dish and the neon tube to prevent unwanted light reflections.

Special care is also taken to protect the system from any sources of perturbations. The dish is surrounded by a transparent plexiglas cylinder of internal radius 9 cm, against air motion. Vibrating apparatus (thermostatic bath and pump) are placed on dampers.

4 Dynamical regimes: a qualitative overview

4.1 Flow structures in the circular fountain

The pattern of columns appears for the flow-rate Γ ranging from 0.05 cm^2/s to 0.7 cm^2/s. At smaller flow-rate, an array of static dripping sites is observed, whereas at higher flow-rate an annular liquid sheet replaces the pattern of columns. The study of annular sheets has been published elsewhere [52].

The transitions between these different flow regimes exhibit hysteresis: the flow-rate above which dripping sites turn into columns is slightly larger than the flow-rate below which columns turn into dripping sites. Similarly, the annular sheet replaces the columns above Γ between

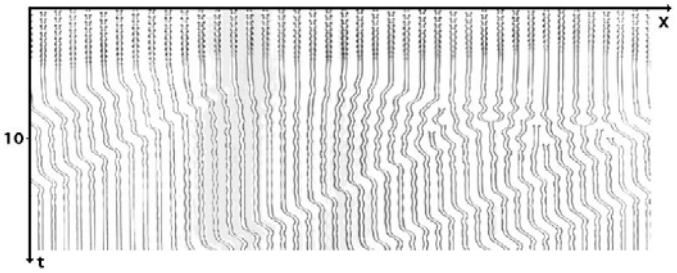

Fig. 4. Transition from dripping sites to columns regime, by increasing the flow-rate ($\eta = 100$ cP). Γ ranges from 0.05 cm^2/s to 0.14 cm^2/s. In the beginning, one notices that dripping sites appear as dashed tracks. Then, columns appear as continuous tracks. On these diagrams, and on the following ones, time is labeled on axis in seconds.

0.6 cm^2/s and 0.8 cm^2/s (the value depends on viscosity), whereas such a liquid bell can be maintained at very low flow-rate once formed: if the flow-rate is carefully decreased and if the sheet is protected from surrounding perturbations, one can maintain the bell at Γ of order 0.01 cm^2/s [52]. Thus, rainbow patterns appear on the surface, witnessing that the liquid thickness is locally equal to a few light wavelengths.

As a consequence of these hysteresis, mixed states are observed, including both dripping sites and columns or columns and a local triangular-shaped sheet, in the same way as it was already observed in an overflowing cylinder experiment by Pritchard [31] and Giorgiutti et al. [32]. The network of dripping sites remains static and has a homogeneous wavelength, which is very close to that of the Rayleigh-Taylor (RT) instability of a thin layer hanging below a solid ceiling [29]:

$$\lambda_{drops} = \lambda_{RT} = 2\pi\sqrt{2}\sqrt{\frac{\sigma}{\rho g}}. \qquad (10)$$

With silicon oil, this wavelength equals 1.30 cm and is independent of the viscosity. Thus, the network of dripping sites is very similar to the case of a simple RT instability.

The natural spacing between columns at rest, is slightly smaller than the RT wavelength. When the flow-rate is increased in order to progressively transit from dripping sites to columns, a transient state is noticed, during which columns simply come up at locations of the former dripping sites. However, the pattern of columns can not withstand a homogeneous static state at this wavelength, and several new columns are then nucleated. This necessary adjustment causes a decrease of the mean wavelength λ_m. The spatiotemporal diagram of Figure 4 illustrates this behavior. Note also that the final state includes three small propagating domains, inside which a part of the remaining dilation remains trapped.

One of the fundamental differences between dripping sites and columns is that the latter are coupled to each other. In other terms, any column of the pattern feels the motion of its nearest neighbors, contrary to dripping sites. This is evidenced by the following fact: when one introduces a needle in a dripping site and tries to drag it by

capillary effects, the resulting motion of the dripping site does not lead to any subsequent motion of the neighboring sites, which remain static. This has to be related to the fact that no dynamical regime has ever been observed in a pattern of dripping sites. On the opposite, the motion of any column is strongly related to its neighbors. The coupling of the motion of nearest neighbors leads to a collective dynamics in the pattern of columns.

In the following, the term 'regime' will refer to dynamical states of the pattern of columns, in opposition to the 'flow regimes' previously used to qualify dripping sites, columns or sheets.

4.2 General description of the dynamics

As already reported in previous articles [22,24–26], the pattern of columns exhibits different dynamical regimes, depending on both the flow-rate per unit length Γ, and the initial conditions. Indeed Γ does not constitute the only quantity governing the state of the system. The state reached asymptotically is strongly influenced by the initial conditions, i.e. the number of columns, their position and velocity. These conditions can somehow be controlled by the experimentalist, using needles to force local motions and spacing, as explained in more detail in previous papers [22–25]. Some of these quantities are dependent on each other: for instance, the velocity of a column is strongly related to the distance to its neighbors.

Practically, with experience and a bit of skill, it is possible to add or delete columns at will, at specific locations on the pattern. One starts from a primary regime of static columns (abbreviated as ST in the following). The detailed description of this manipulation is related elsewhere [22,23], but can be summarized here in two main cases:

- one can bring two neighboring columns to each other, in a quasi-static way. In that case, a column can be locally suppressed without any initial speed. This technique is used to change the number of columns and to keep the pattern static, or to turn a static state to an oscillating one. In the same way, one can slowly move two columns away from each other, and provoke the nucleation of a new one between two others.
- one uses a needle to drag a column at a certain speed, towards one or several neighboring columns. Then, some of these columns are suppressed by coalescence and several others acquire an initial speed that equals the speed of the needle. This technique is rather used to create propagative domains. Providing that the drag speed is included in a certain range, the drag speed and the drift velocity selected asymptotically by the system are the same. This technique enables a selection of the size of the domain and of the drift velocity, independently from each other. For example, it is possible to create a domain of drifting cells that extends to the whole dish [22,24], if a large number of columns are suppressed in that way. Depending on the speed one uses to drag columns with the needle, a different wavelength is obtained inside the final domain: the larger the speed is, the larger the obtained wavelength. Then, this enables to control the wavelength in a certain allowed range.

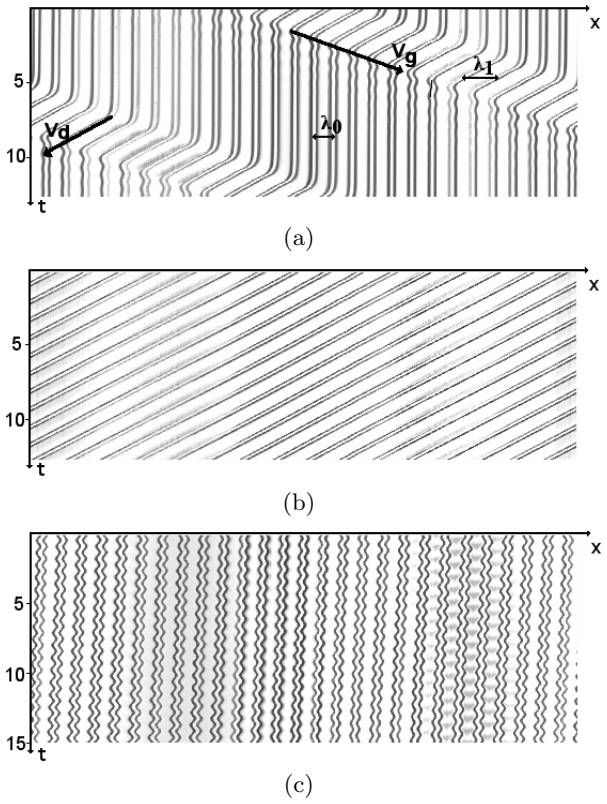

Fig. 5. Overview of the main dynamical regimes ($\eta = 100$ cP). (a) Localized propagative domain (LD) followed by transient oscillations ($\Gamma = 0.15$ cm^2/s). One defines the quantities V_d (drift velocity), V_g (wall 'group' velocity) and the wavelengths inside and outside the domain λ_1 and λ_0. (b) Global drifting state (GD) ($\Gamma = 0.19$ cm^2/s). (c) Extended oscillating regime (OSC) ($\Gamma = 0.21$ cm^2/s).

Spatio-temporal diagrams of the main obtained states are shown in Figures 5a–5c which represent successively a localized domain (LD) propagating endlessly along the dish, a globally extended drifting state (GD) and an extended oscillating state (OSC). These regimes are ubiquitous in similar systems, like the printer's instability [8,10] or directional solidification [12–15]. In the LD case, it appears that the wavelength outside the domain is selected to a certain value λ_0, by a robust process: indeed λ_0 does not depend on the flow-rate Γ, on the size of the domain, on the velocities V_g and V_g or the wavelength inside the domain λ_1. Only fluid parameters like viscosity or surface tension seem to influence it [24,25,48]. Such a wavelength selection has also been noticed in other systems, like the printer's instability or directional solidification [8,14].

Besides these well-known behavior, the oscillating-drifting state (OSD), only briefly reported previously [26], can roughly be viewed as made of successive identical small propagative domains. It is then closely related to localized drift. Furthermore, this state has the remarkable

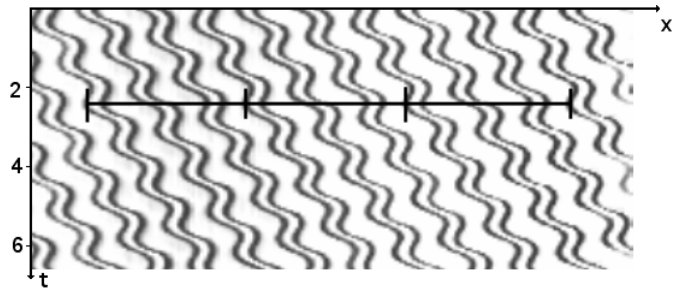

Fig. 6. Spatial tri-periodicity in the oscillating-drifting state (OSD) ($\eta = 200$ cP, $\Gamma = 0.25$ cm^2/s).

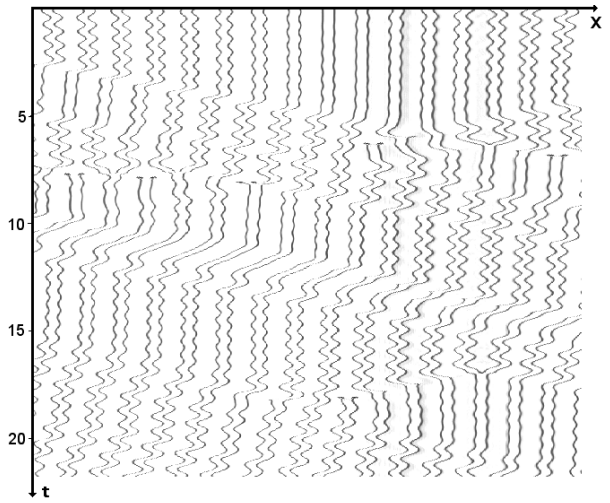

Fig. 7. Regime of spatiotemporal chaos (STC) ($\eta = 100$ cP, $\Gamma = 0.25$ cm^2/s).

property of leading to a tripling of the spatial wavelength. In other words, the motion of a given column is the same on every third column as suggested in Figure 6. This state is similar to the so-called 'T-xλO' (Tilt extended wavelength Oscillations) states reported in directional solidification of thin layers of eutectics [15]. In our case, $x = 3$.

Besides these latter regimes that should be qualified as 'ordered', 'predictable' or 'laminar', the system exhibits chaotic regimes in a certain parameter domain. In these regimes, chaos is both temporal and spatial (see Fig. 7), hence called spatiotemporal chaos (STC). The columns have chaotic motion and the number of columns N is not constant. It means that two neighboring columns can meet in their erratic motion and can merge spontaneously, and that a column can also spontaneously split in two. By analogy with streamlines in usual channel flows, this type of regime is often qualified as 'non-laminar' or 'turbulent'. Of course, the word 'turbulent' does not refer to the motion of elementary fluid particles which remain laminar, but rather to the spatial phase variable ϕ describing the positions of columns. Each event such as the merging of columns, or the splitting of a column, represents a singularity for the spatial phase of the pattern. These events are called 'defects' here and in our previous papers. In one of these previous papers, we have shown that they contribute to sustain chaotic motion, and that their spatiotemporal density is a good measurement of disorder [26]. These defects are produced by interactions between dynamical states, for example oscillations and domains of drifting columns. No chaotic motion can be observed if there are no such defects in the structure. In other words, the number of columns is necessarily a fluctuating quantity in a chaotic state.

The conditions for obtaining the different regimes are detailed in the next paragraph, in the form of stability diagrams.

4.3 Stability diagrams

We study regimes that are obtained when one varies the three available parameters: the flow-rate Γ, the mean wavelength λ_m and the viscosity η. Γ can be selected between 0.005 cm^2/s, up to 1 cm^2/s. The mean wavelength λ_m is controlled through the number of columns N, as $\lambda_m = \pi D/N$ (D being the diameter of the circle along which columns travel), and thus it takes discrete values. Its usual range of value is between 0.95 cm and 2.5 cm. Silicon oils of different viscosity have been used, keeping the surface tension constant, see Table 1. The resulting diagrams are depicted in Figures 8–10 respectively for the 20 cP, 100 cP and 200 cP silicon oil. From these diagrams, several comments can be drawn up:

– At 100 and 200 cP, the threshold for transition to STC is almost the same for both viscosities: $\Gamma_{STC} = 0.34$ cm^2/s. It is worth giving a significance for Γ_{STC}, as one can clearly observe that several ordered states still exist at much higher flow-rates, for instance GD at large λ_m or ST at small λ_m. These states correspond to specific situations that are never spontaneously obtained, but are rather carefully 'prepared' by the experimentalist (see Sect. 4.2, above). The threshold Γ_{STC} is meaningful for the other usual conditions, practically most of the conditions. Thus, when one starts from an initially chaotic state, the latter will turn laminar after a finite time if the flow-rate is decreased below Γ_{STC}. Also, from random initial conditions (practically when the dish starts to overflow), the system converges towards an ordered state if $\Gamma < \Gamma_{STC}$ (after a more or less short transient), whereas it stays endlessly chaotic $\Gamma > \Gamma_{STC}$ [26].

– At 20 cP, the diagram is quite simple: a large domain of static states (ST), and narrow domains for LD and GD. At 50 cP, the diagram is qualitatively the same, with larger domains for LD and GD and a smaller domain for ST. Let us mention that for even lower viscosities, the system mainly lies in a static state. Some preliminary experiments carried out at 10 cP showed a very narrow range for dynamical regimes, and practically it was very difficult to keep them stable for reliable measurements.

– The most complex dynamics is obtained for larger viscosities. STC regimes are observed for 100 and 200 cP. Furthermore at these viscosities, the existence range of ST states is narrow, whereas those of LD and GD are much extended. At 200 cP, the new OSD state is observed when a transient chaotic regime turns to a laminar one, Γ

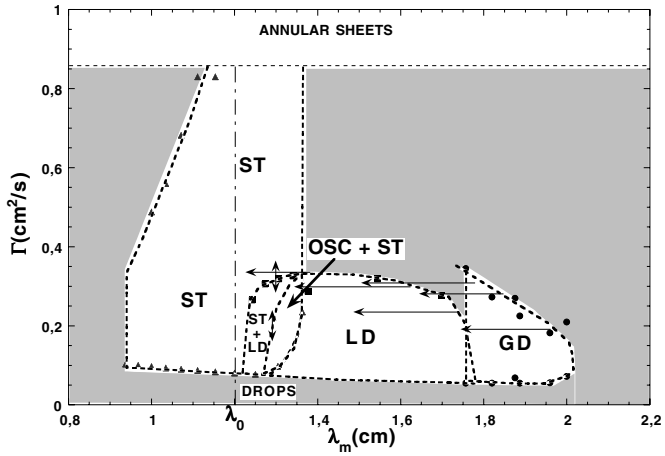

Fig. 8. Stability diagram at $\eta = 20$ cP (see text for notations).

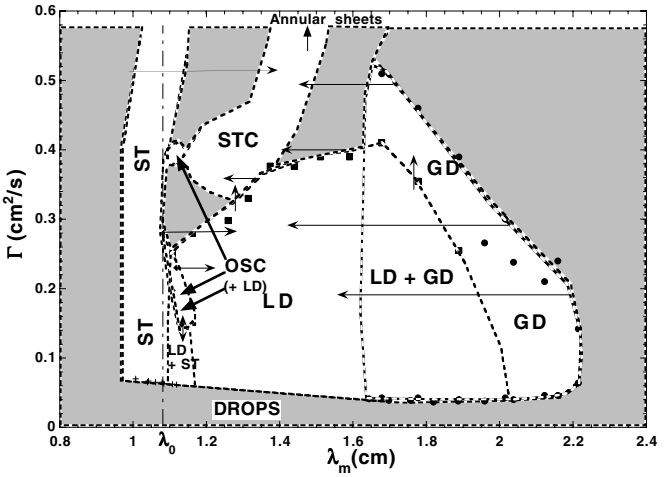

Fig. 9. Stability diagram at $\eta = 100$ cP (see text for notations).

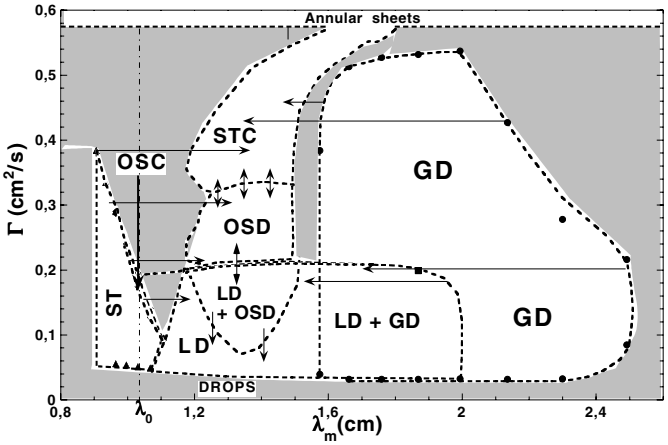

Fig. 10. Stability diagram at $\eta = 200$ cP (see text for notations).

being slightly smaller than the threshold for chaos Γ_{STC}. It turns out that this is the only stable state in a narrow range of flow-rate just below the threshold of chaos. But once obtained (waiting long enough that the disordered transient turns into this state), such a state can be maintained in a large range of Γ.

– The STC regime only appears at high enough viscosity: a minimal viscosity of η around 100 cP seems to be necessary, as no permanent chaotic states could be obtained at a viscosity of 90 cP. Under those conditions, there exists a domain of parameters (Γ, λ_m) where the pattern cannot reach a predictable, asymptotically stable state, but instead behaves chaotically, as shown in Figure 7. Various breakup scenarios are observed as one crosses the boundary of the STC domain, starting from an ordered state. The main results obtained in the STC regime have been reported in a previous article [26].

– In Figures 8–10, arrows represent the transition from a state to an other. When a double arrow, it means that the transition is reversible, which means λ_m keeps constant. Most of the transitions are not reversible, as they induce a change of N. Then, since this change is induced by a variation of Γ, it is not possible to return to the previous state by proceeding the opposite variation of Γ. For the very few reversible transitions, a return to the previous state is possible by simply varying the flow-rate back to its initial value. For non reversible transitions, there is not even a hysteresic behavior, as the return to the initial state would require to rebuild the suitable initial conditions (number and position of columns) in order to reach it. For example in Figure 9, the arrow starts at the boundary of a GD state, and ends in LD or STC domains. It means that the latter GD state has been broken and has turned to another state, generally with a shorter λ_m.

– The OSC domain has different shapes, depending on the viscosity. At 20 cP, the existence domain is quite large and localized at low flow-rates, and thus in some sense the system stabilizes when increasing Γ . At 200 cP, extended oscillations appear in a very narrow range of flow-rate although they appear for a larger range of λ_m. At 100 cP, the domain splits in two small parts. The upper part can be reached by starting at low Γ with a suitable wavelength, and by increasing abruptly Γ in order to skip the unstable area in between.

– Some domains of parameters allow the existence of several distinct states, for instance LD+GD, LD+OSC, LD+ST, ... It does not mean that two different states coexist at the same time, but rather that two different states are possible in that range of parameters. The occurrence of one state or another one depends on initial conditions, i.e. position and speed of columns.

5 Quantitative study of dynamical regimes

5.1 Static states and wavelength selection

As stated in the previous section, ST states are obtained with a large number of columns N, i.e. a small λ_m. As shown in the stability diagrams, the range of λ_m where they exist, is almost independent on Γ at low flow-rate and shrinks at higher flow-rates.

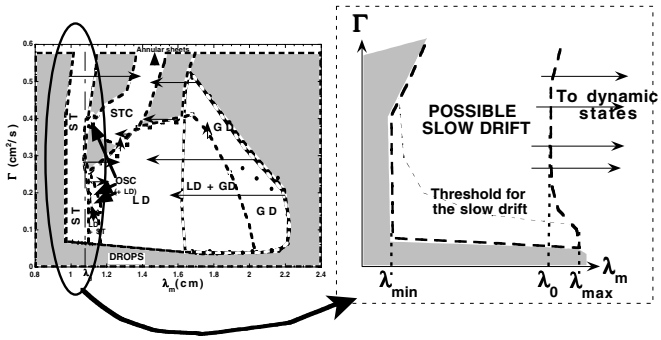

Fig. 11. Schematic close-up around the range of existence of static states (100 cP).

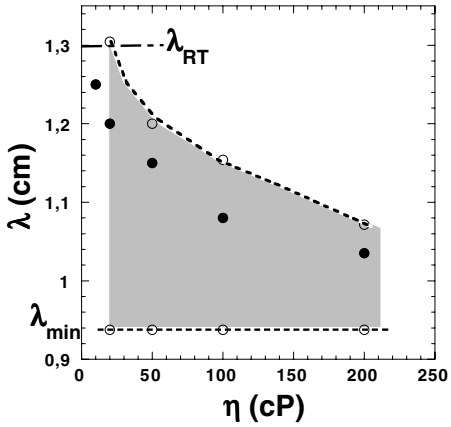

Fig. 12. Range of wavelength where static states are stable, versus viscosity. Black circles represent the reference wavelength λ_0. Open circles stand for the boundaries λ_{min} and λ_{max} at low Γ.

This is apparently the simplest state as it follows from the primary instability, before any secondary bifurcation takes place. At the very first stages of its setting in, slow transient motions have been observed. These slow motions do not last more than one minute. They tend to equalize the wavelengths. However, they seem to play a role in the further appearance of a global slow drift of the pattern. Indeed, it has been noticed that a state of slow drift could appear from a static state if Γ overcomes a certain threshold, as it will be presented later in the paper. A possible way to kill occurrences of the slow drift, is to let the pattern turn perfectly homogeneous in space, by waiting for the phase diffusion to be achieved. To proceed so, the flow-rate has to be kept below the threshold value Γ_{cs} during a while: typically one minute after the primary stage of overflowing. Under this condition, the pattern will stay frozen even for Γ higher than the usual threshold. However in this situation, a slow drift can be turned on anyway, providing that a suitable perturbation is brought to the pattern: for instance, by dragging columns very slowly with a needle, and thus by initiating the expected motion. In that sense, the bifurcation towards slow drift can somehow be considered as sub-critical. Measurements of this state are presented later in the section. A close-up to static and quasi-static (with slow drift) states is presented in Figure 11.

The wavelength λ_0 that is selected in the wake of a propagative domain (Fig. 5a), is also almost independent on Γ. However both the range of ST and λ_0 depend on viscosity η. This dependency is reproduced in Figure 12.

Some further comments can be extracted from Figures 11 and 12:

- λ_0 is always lower than the theoretical RT wavelength λ_{RT}, and decreases as η is increased. At small viscosity, λ_0 approaches λ_{RT}.
- The range of λ_m for stable ST states becomes narrower at large viscosity, as those states become less and less prevalent. However, the minimal wavelength λ_{min} does not vary, and nearly equals the minimal wavelength for which the growth-rate of the RT instability is positive, i.e. $\lambda_{min} = 2\pi\sqrt{\sigma/\rho g} = \lambda_{RT}/\sqrt{2}$ [29]. Thus any attempt to add a column when the system lies at λ_{min} provokes the merging of two columns somewhere else in the pattern: so the system keeps itself above λ_{min}.
- At the other end of the stability domain (Fig. 11), the ST states bifurcate towards dynamical ones (OSC or LD) when it crosses the stability limit. λ_{max} is generally smaller than λ_{RT}, except at lower viscosities when it becomes equal to this limit value, see Figure 12.
- The value λ_{max} is larger than λ_0 at low flow-rate: this is the plotted value in Figure 12. At higher flow-rate, λ_{max} is close to λ_0. As a consequence, oscillations at the trailing edge of LD states become unstable and cause their break-up.

In view of the relative simplicity of the basic static pattern (liquid columns connected by a liquid film), it is tempting to seek for possible interpretations of its structure with standard hydrodynamic theory of thin film flows, namely the lubrication theory [53]. In a previous paper [52], we have shown that the liquid thickness of the film flowing down the vertical edge of the dish (see Fig. 3) was behaving as: $e \sim (\frac{\eta}{\rho g d})^{1/3}\Gamma^{1/3}$, then in agreement with the lubrication theory [53]. Does this also hold for other regions of the flow, for instance for what concerns the liquid layer hanging just below the dish? An attempt for answering this question is detailed in Appendix A, that shows how far simple dimensional arguments can lead in such a system. Particularly, a prediction of h, the thickness of the liquid layer of an arch between two columns is proposed, and confronted to measurements.

5.2 Oscillatory state with spatial period-doubling

Out-of-phase oscillations appear when the local wavelength is slightly larger than λ_0. This situation can occur (a) globally on a homogeneous state with a suitable number of columns (Fig. 5c); or (b) locally at the trailing edge of a propagating domain of drifting columns (Fig. 5a). As suggested in stability diagrams (Figs. 8–10), situation (a) occurs in a narrow range of parameters. Figure 13a shows measurements of angular frequency ω versus Γ, for various viscosities from 10 cP to 200 cP, obtained for both

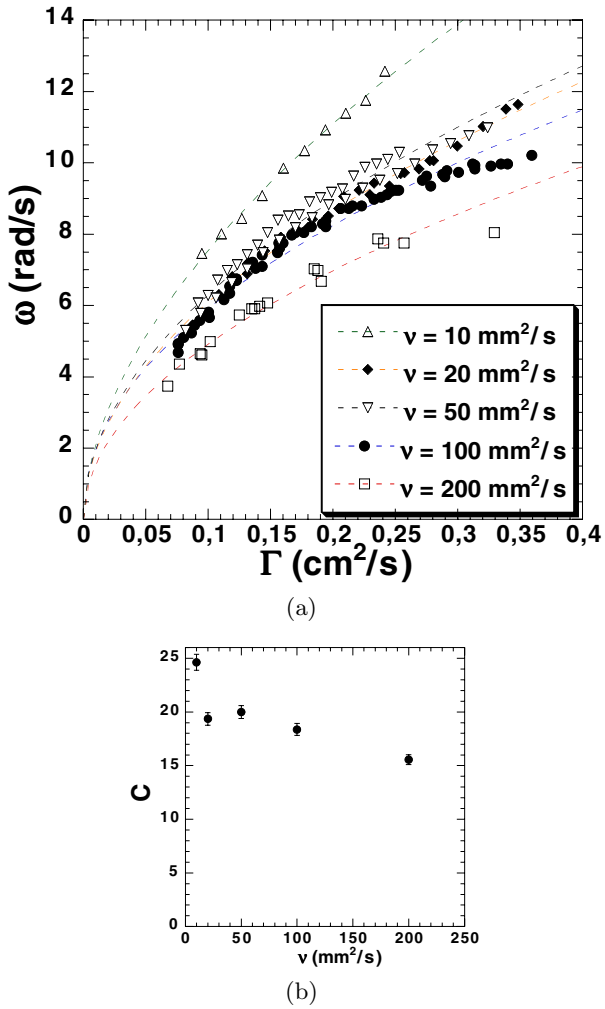

Fig. 13. (a) Angular frequency of oscillations versus flow-rate, for different viscosities. Dashed curves stand for data fitting by a square-root function of flow-rate: $\omega = C\Gamma^{1/2}$. (b) Value of C versus viscosity.

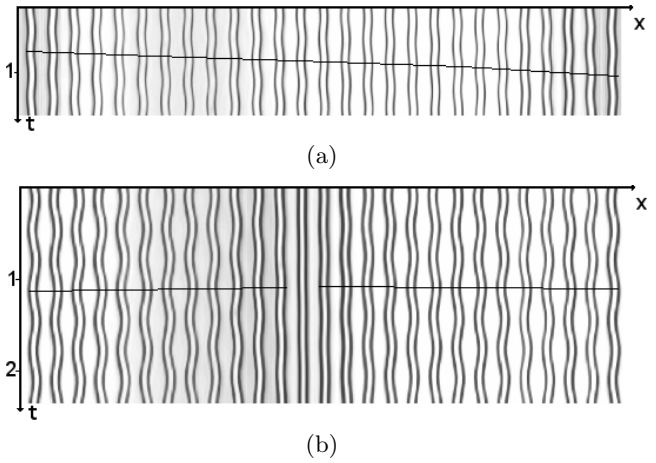

Fig. 14. Phase and amplitude inhomogeneities in an extended oscillating regime with a odd-number of columns ($\eta = 100$ cP, $\Gamma = 0.26$ cm^2/s, $d = 10$ cm, 27 cols.). (a) Progressive phase drift along the pattern. (b) Steep phase jump coinciding with an amplitude hole.

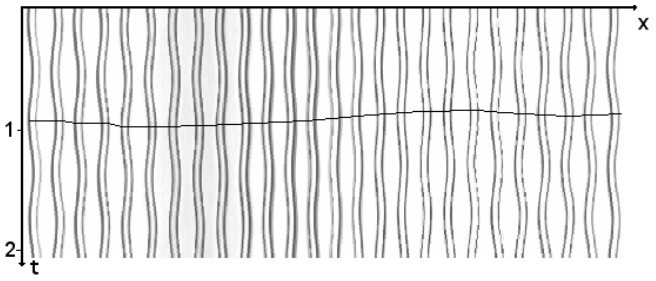

Fig. 15. Almost homogeneous amplitude in an extended oscillating regime, without any phase jump. 26 col. $\Gamma = 0.18$ cm^2/s, $\eta = 100$ cP. Duration 2 s.

situations (a) and (b). No difference in ω could be noticed between measurements obtained in both situations (see [25]).

At any given viscosity, data are well fitted by a square-root law: $\omega = C\Gamma^{1/2}$. Figure 13b shows the evolution of C with viscosity.

The simple empirical relationship $\omega \sim \Gamma^{1/2}$ suggest that this law should be obtained from a coarse argument, based on the seek for characteristic length and time. This is detailed in Appendix B.

5.3 On phase inhomogeneities inside extended oscillating regimes

A closed-up view on extended oscillating regimes shows that two consecutive columns never oscillate perfectly out-of-phase. It is straightforward that a homogeneous phase profile will not match the periodic boundary conditions if the number of columns is odd. This is illustrated in Figures 14 with $d = 10$ cm, $\eta = 100$ cP and $N = 27$. The black line stands for an isophase in regards to the period-doubling mode. Figures 14a and 14b show two different situations where phase mismatch is observed. Figure 14b shows a sharp phase jump that coincides with an amplitude hole. This behavior has also been observed in experiments of directional solidification [15] and in simulations of coupled amplitude/phase model [40,41].

Under the same experimental conditions ($d = 10$ cm, $\eta = 100$ cP), it is possible to obtain an extended oscillating regime with an even number of columns ($N = 26$). Only smooth variations along the isophase can be noticed, see Figure 15.

However, an amplitude hole can exist with an even number of columns. In this case, its occurrence can be coupled to a global slow drift, as illustrated in Figure 16, and it seems that the amplitude hole corrects the phase mismatch resulting from the slow drift.

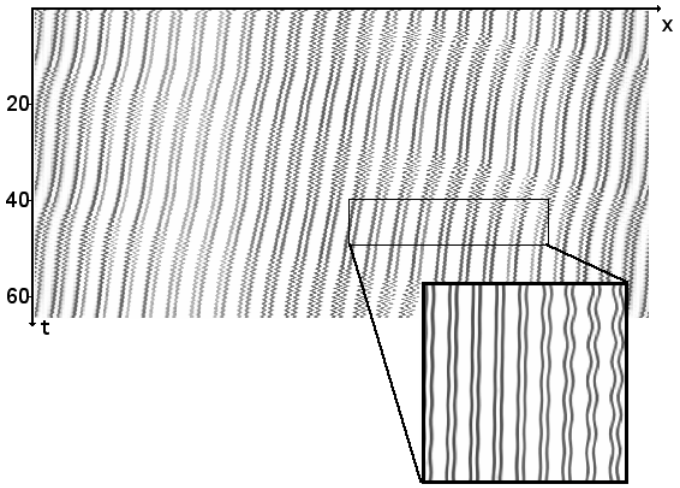

Fig. 16. Drifting amplitude hole in an oscillating state. 26 col., $\Gamma = 0.139$ cm^2/s, $\eta = 100$ cP. Duration 64 s. The close-up shows local variations of the amplitude.

5.4 Global drifting states: a quantitative study of parity-breaking

The main feature of this system is the possibility to perform exhaustive and accurate studies of the parity-breaking bifurcation. In this section, we investigate the phase velocity of the parity-broken states, when these states cover the whole pattern (GD states). We also interpret the observed results in terms of coupled amplitude and phase equations, in the spirit of Goldstein et al. description [36]. A brief account of this work, has been published in [24].

As suggested in stability diagrams, GD states can be obtained with a large number of different wavelengths. The wavelength being simply equal to $\lambda = 2\pi d/N$, it is possible to tune it by changing N, in order to study separately the influence of flow-rate, viscosity and wavelength on V_d. Measurements are shown in Figures 17a and 17b, where V_d is plotted versus Γ for different viscosities ($\eta = 20$, 50, 100 and 200 cP). They have been obtained with dishes of diameter $d = 10$ and 16.7 cm. For the sake of clarity, each graph shows measurements for only two values of viscosities.

Each branch corresponds to a fixed number of columns, hence a fixed wavelength. The drift velocity V_d is uniquely defined by giving flow-rate, viscosity and wavelength. It is a growing function of wavelength and of viscosity. It increases sharply at low flow-rate, tends to saturate at medium flow-rate and slightly decreases at high flow-rate.

Detailed measurements for one value of viscosity ($\eta =$ 100 cP) are shown in Figures 18a, 18b. Figure 18a shows values of speed V_d. Figure 18b represents the square of the quantity $(V_d k)$, which is also the square of the time derivative of the spatial phase (ϕ_t), see Section 2. This quantity exhibits a linear dependency with flow-rate, in a significant range above threshold. The threshold Γ_c is defined as the value of flow-rate extrapolated to $V_d = 0$. Such a dependency is predicted by the model of Goldstein et al. [36] for a supercritical bifurcation towards a parity-broken state. However these measurements show that both the slope and threshold depend on λ, which was not included in their initial model. From this set of measurements, it has been possible to determine coefficients of the model of equations (4) and (5), and furthermore to propose the addition of new terms.

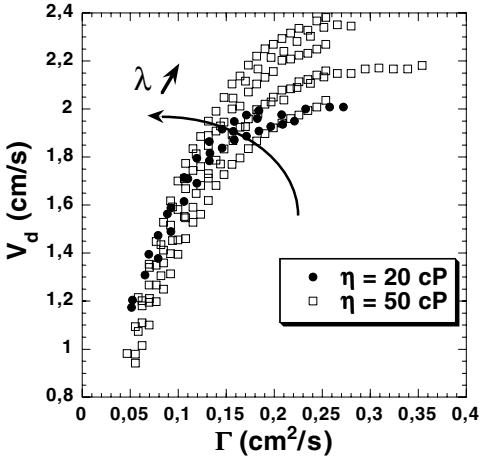

(a)

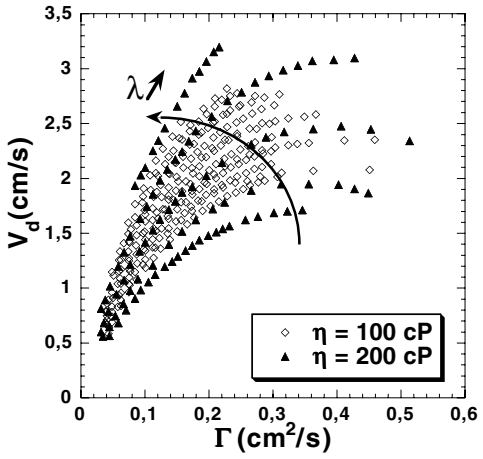

(b)

Fig. 17. Phase velocity V_d of a global drifting state, for various wavelengths λ. (a) $\eta = 20$ and 50 cP. (b) $\eta = 100$ and 200 cP.

Defining a and Γ_c respectively as the slope on Figure 18-b and the flow-rate threshold, one can write an empirical law as follows:

$$\phi_t^2 = (V_d k)^2 = a(\phi_x)(\Gamma - \Gamma_c(\phi_x)). \tag{11}$$

The quantity ϕ_x, defined in equation (6), represents the spatial derivative of the phase. It is negative inside a domain of drifting, dilated cells. For all viscosities studied, a and Γ_c exhibit linear variations with ϕ_x as seen in Figures 19a, 19b for $\eta = 100$ cP.

The following relationships result:

$$\Gamma_c(\phi_x) = \Gamma_{c0} - \kappa\phi_x \tag{12}$$

$$a(\phi_x) = \alpha\phi_x + \beta. \tag{13}$$

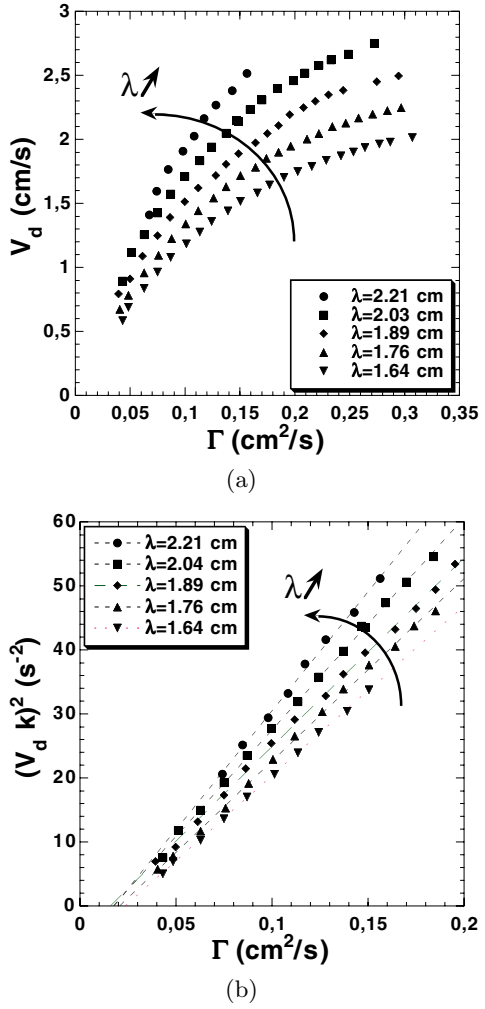

Fig. 18. (a) V_d measurements for $\eta = 100$ cP, and for different wavelengths. (b) Square of the time derivative of the spatial phase $\phi_t^2 = (V_d k)^2$.

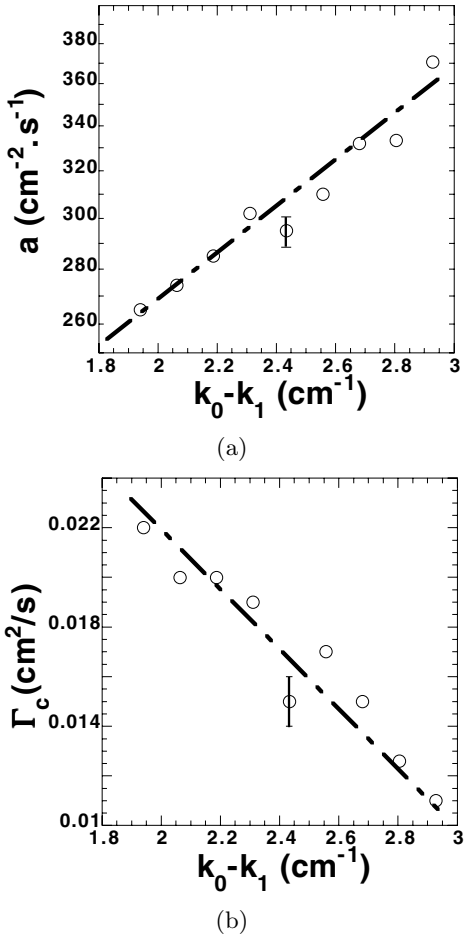

Fig. 19. Constitutive parameters of the predictive law for the phase dynamics, obtained from coupled amplitude/phase equations ($\eta = 100$ cP). (a) Coefficient a, versus $k_0 - k_1 = -\phi_x$ and (b) Threshold Γ_c.

Measurements with four values of viscosities allow to roughly capture the evolution of α and β with η, see Figure 20a: β decreases significantly as the viscosity increases, whereas α shows a slight increase around a value of –100.

The quantities κ (which has the dimension of a flow-rate) and Γ_{c0}, appearing in the empirical expressions of the threshold, are both decreasing with viscosity as power laws (of respective exponents –0.41 and –0.94), see Figure 20b. This means that: (1) a high viscosity tends to promote the instability at a fixed flow-rate. (2) the threshold is less and less wavelength-dependent at high viscosity.

In a previous paper [24], we showed that it was possible to turn these empirical results into a rigorous adjustment of Goldstein et al. model (Eqs. (4) and (5)). We proposed to add new terms that are consistent with the symmetries of the system, which allows to recover our results. The following extended model is the simplest that reproduces experimental data [24]:

$$A_t = (\mu + \epsilon\phi_x)A + \gamma A_x A + DA_{xx} - \nu(\beta + \alpha\phi_x)A^3 + ... \quad (14)$$

$$\phi_t = \nu(\beta + \alpha\phi_x)A + D_\phi \phi_{xx} + ... \quad (15)$$

by identifying μ to $(\Gamma - \Gamma_{c0})/\nu$ and ϵ to κ/ν. Let us note that ν has the dimension of the square of a length: its numerical value can be chosen equal to one without any loss of generality.

These equations include new terms that couple the amplitude and the phase gradient: the coefficients ζ and δ of (9) are linear functions of ϕ_x. All the terms in these equations match with the symmetries of the primary pattern (namely $x \to -x$, $\phi \to -\phi$, $A \to -A$): any of these terms will turn to its opposite by the latter transformation.

5.5 Propagative domains of drifting cells: range of existence and kinematic properties

In a GD state, the wavelength can be selected at will by the experimentalist via the number of columns N,

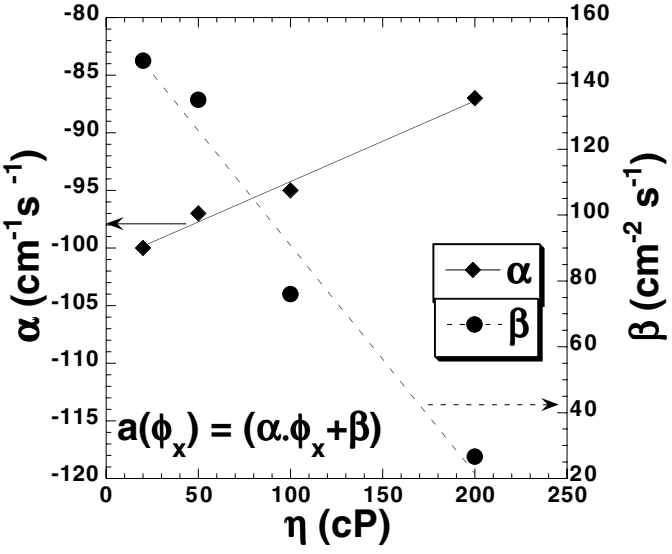

(a)

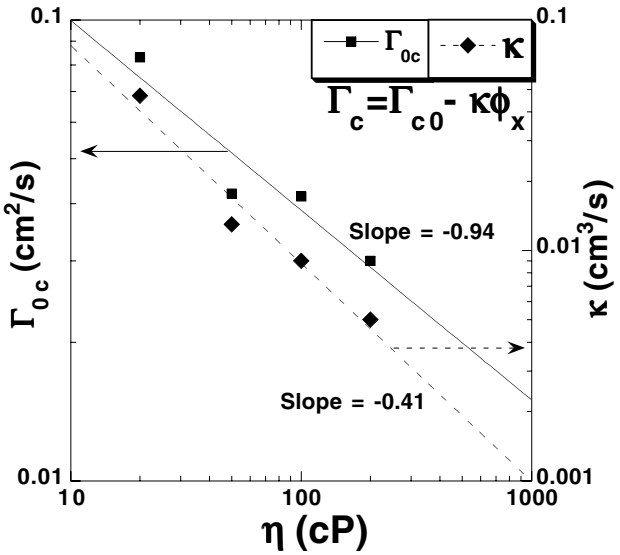

(b)

Fig. 20. Coefficients of the model (14)(15).

as: $\lambda = 2\pi R/N$. In a LD state, λ is selected by the system itself, as well as the wavelength selected outside the domain λ_0.

In order to clarify the wavelength selection process inside and outside a LD, it is worth approaching their range of existence presented above in Figures 8–10, but replacing λ_m by the phase gradient ϕ_x. Figure 21 represents the phase gradient inside a domain for various LD states, versus flow-rate. The dotted line represents the stability limit of GD states. Except for high flow-rate, the wavelength of standing columns outside domains is equal to the reference one: $\lambda_0 = 1.08$ cm with the silicon oil of $\eta = 100$ cP. For most of the LD states, the phase gradient is surrounded by the boundaries of GD states. There exists anyway a few measurements at small λ_1 showing abnormally small phase gradients and lying out of the GD existence domain. Otherwise, the range of existence for (ϕ_x,Γ) is larger for GD than for LD. Global states are constrained to a fixed wavelength, whereas LD states can adjust their wavelength dynamically. This adjustment, provoked for instance by a modification of Γ, apparently occurs before the bounds of the GD existence domain are reached, as shown in Figure 21.

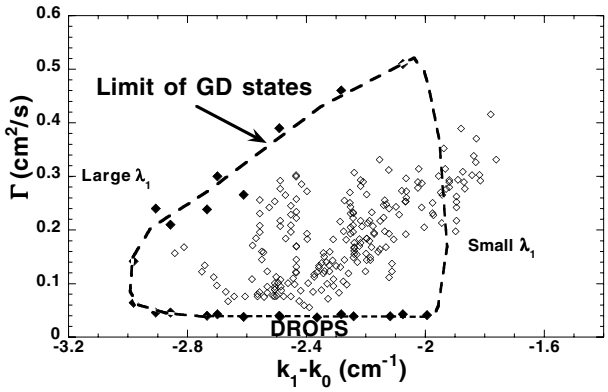

Fig. 21. Range of existence of domains of drifting cells, in gradient of the space phase ϕ_x versus flow-rate ($\eta = 100$ cP). Open symbols stand for LD states, filled symbols and the dotted line bound the stability domain of GD states.

This suggests that the wavelength selection inside a domain is somehow more subtle than what was reported in previous studies [23]. Indeed, the wavelength λ_1 is primarily chosen in a large range of values, depending on how the domain is generated. Then, the chosen value will be kept until a significant change on the values of control parameters is applied, so that the system can not hold the initial wavelength anymore and adjusts itself to another value. Such a change can be an increase of Γ or the creation of another domain.

Let us now present the kinematic properties of LD states. Figures 22a–22c present measurements of wavelengths λ_0 and λ_1, group (V_g) and phase (V_d) velocities for various acquisition series, on domains of various sizes, with a viscosity of $\eta = 100$ cP. Other measurements have been performed as well for different viscosities, and have revealed similar tendencies.

Like for GD states, V_d increases with flow-rate. So does the group velocity V_g. Data have been obtained from localized domains of different sizes and different internal wavelengths λ_1. The size has no influence on velocity, but λ_1 influences V_d and V_g. As previously presented in Figure 21, λ_1 can take various values for the same flow-rate. The same kind of dispersion is observed for V_d and V_g values. However, it is confirmed that λ_0 is almost constant within the studied range of flow-rate, and thus constitutes a suitable reference wavelength.

Let us write the kinematic relationship of the forward or backward fronts of a localized domain [14]:

$$\frac{\lambda_1}{\lambda_0} = 1 + \frac{V_d}{V_g}. \tag{16}$$

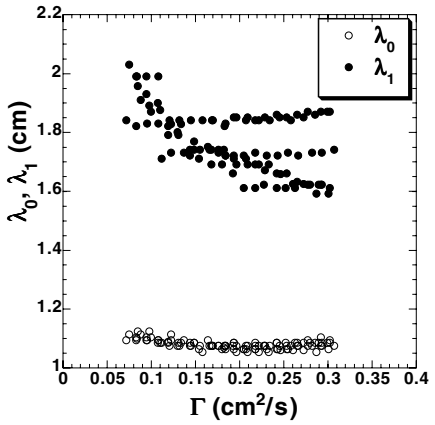

(a)

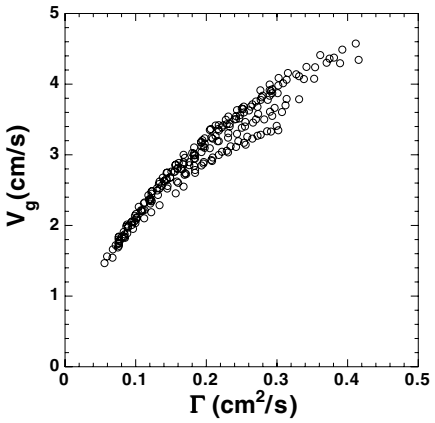

(b)

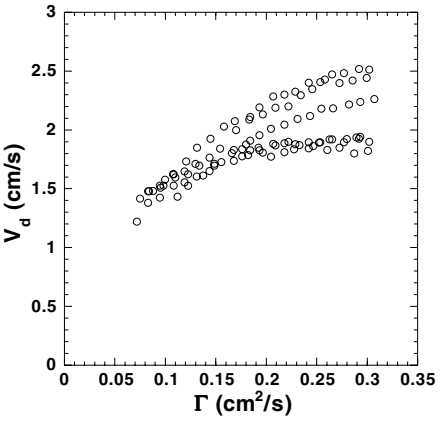

(c)

Fig. 22. Measurements on propagative domains ($\eta = 100$ cP). (a) Wavelengths versus flow-rate. (b) Group velocity versus flow-rate. (c) Phase velocity versus flow-rate.

Or written differently:

$$V_d k_1 = -V_g \phi_x. \tag{17}$$

This suggests that if one wants to unify all the measurements, one needs to check the dependency between V_d and λ_1. Let us recall that λ_1 can not be controlled inside a localized domain, contrary to the case of GD states, and that

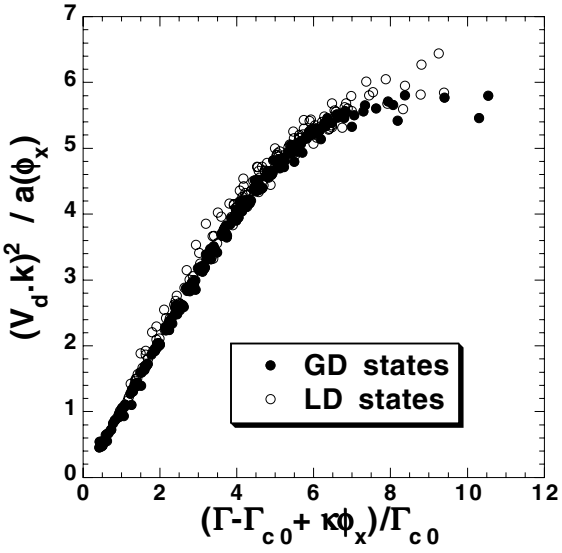

Fig. 23. Rescalling of measurements of V_d on a single master curve.

it stays bounded in a flow-rate-dependent range, as shown in Figure 21. One can explain the dispersion on V_d and V_g by the dispersion on λ_1. Using the same scaling-laws as for GD states, it is possible to make data for V_d and V_g collapsing on a single master curve. Figure 23 shows data for V_d for both LD and GD states, corresponding to Figures 18 and 22c, and rescaled with the quantities defined by equations (12) and (13). The scaling law holds very well, even far from threshold. The same scaling is possible for V_g, using equation (17): the collapse of V_g measurements on a single curve is obtained by plotting the quantity $V_g \phi_x (\alpha\phi_x + \beta)^{-1/2}$ versus $\Gamma - \Gamma_c(\phi_x)$, see Figure 24.

From these scalings, it is possible to draw some short conclusions. First, it appears that localized domains and global states have the same kinematic properties, the only difference being that the system chooses itself the wavelength inside a localized domain. Secondly, if the pattern includes several domains, they will necessary have the same λ_1 and V_d, as they have to propagate at the same speed V_g, so that no domain can go ahead of another one.

5.6 Oscillating-drifting state: quantitative study

As briefly mentioned in Section 4, the OSD state can be obtained under quite specific conditions. First, a high viscosity is needed: it was mainly observed for $\eta = 200$ cP, see Figure 10. It could be created and kept stable for $\eta = 100$ cP as well, although in a very narrow range of parameters: this range of appearance was too narrow and not reproducible enough to trace a specific domain for it anyway. It is called 'oscillating-drifting', as can be viewed as successive small, equally sized domains which propagate at the same speed. As each small domain lets a short oscillatory wake (of half a period of oscillations) at its trailing edge, the global motion of a column is a mix between oscillations and drifts.

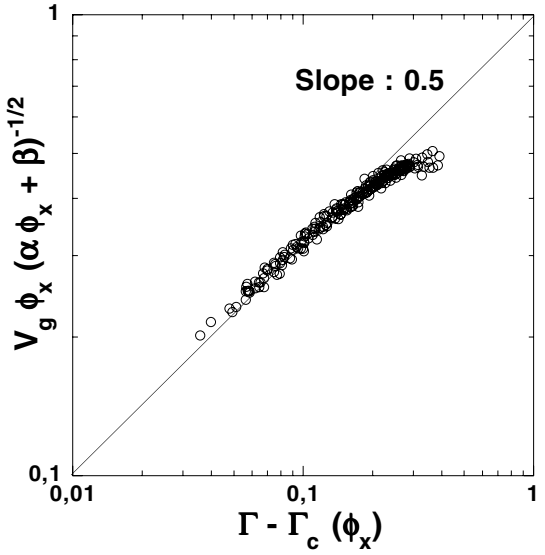

Fig. 24. Rescaling of measurements of V_g on a single master curve (Logarithmic axis).

Such a state appears after long chaotic transients: for $\eta = 200$ cP, there exists a range of flow-rate where the transiently chaotic system can not but reach the OSD state. In a first stage, one lets the system 'quenched' in a permanent STC regime, then one decreases Γ until it is slightly smaller than the critical flow-rate Γ_{STC} (see stability diagram in Fig. 10, and Ref. [26]). Figure 25 illustrates how a transient chaotic state can turn into a OSD state. Once formed, it is possible to keep this state stable into a broad range of Γ, and to perform measurements of its properties. In that sense, the domain of existence is much more extended than the domain of creation. The appearance of such an organized state, without any precursor sign, remains to be explained.

Figure 26a presents the definitions of three characteristic velocities: the group velocity V_g is the same as for a classical propagative domain; but one can define two drifting speed: the maximal drifting speed V_{dmax}, corresponding to the usual speed of a column inside a domain, and the mean drifting speed V_{dmean}. The small domains constituting this state, can co-exist with another domain of larger size (Fig. 26b), and propagate at the same speed.

In the same way as an oscillatory state could exhibit a quasi homogeneous period-doubling only for an even number of columns, the oscillating-drifting state is homogeneous only is the number of columns is divisible by 3. With the dish of diameter $d = 10$ cm for instance, it appears for $N = 23$, 24 and 25; the state is homogeneous and shows perfect tri-periodicity only for $N = 24$.

Measurements for the three velocities defined in Figure 26a are plotted on Figures 27a–27c, for three values of mean wavelength. The velocities increase with flow-rate and with the mean wavelength, which is similar to what is observed on isolated propagating domains. The group velocity is well fitted by a power-law of exponent one half. Figure 27d is the ratio between V_{dmax} and V_{dmean}. This ratio is about 3.

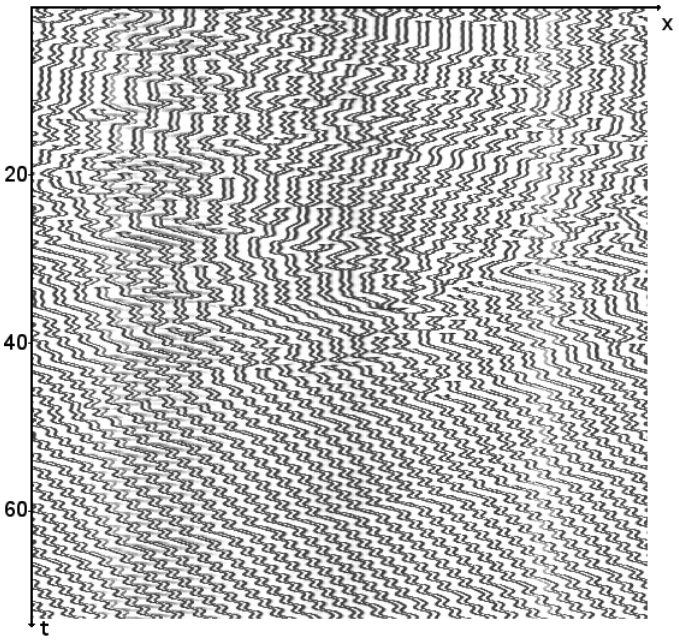

Fig. 25. Convergence of an initially chaotic state towards a particular state (OSD) mixing oscillations and drift. $\Gamma = 0.26$ cm^2/s, $\eta = 200$ cP. The total duration is around 70 s.

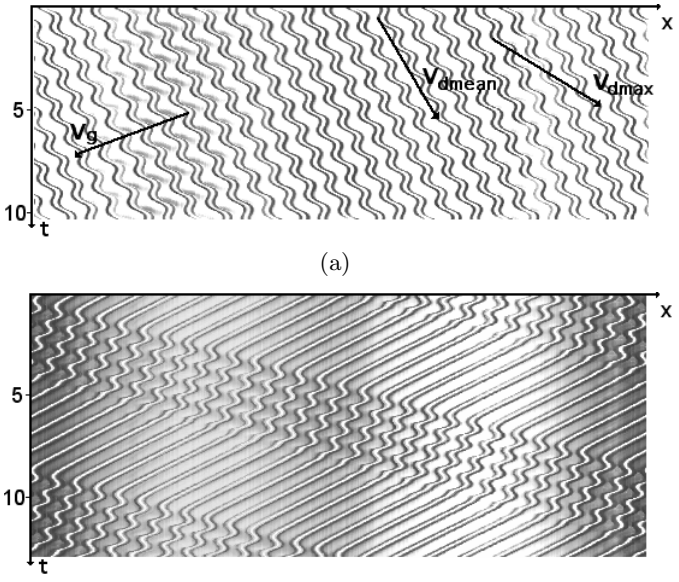

Fig. 26. (a) Oscillation-drifting state, extended on the whole pattern ($\eta = 200$ cP, $\Gamma = 0.242$ cm^2/s, $d = 10$ cm, $N = 24$) and definition of the three characteristic velocities of this state. (b) Co-existence with a local domain of drifting cells. $\eta = 200$ cP, $\Gamma = 0.34$ cm^2/s, $d = 10$ cm, $N = 21$.

5.7 Slow drift of quasi-static regimes

As previously stated, this regime consists in a slow drift of the whole pattern. It can be perceived during long observations of quasi-static states. The typical order of magnitude of the drifting speed V_d is 0.01 cm/s. This regime generally appears when the flow-rate exceeds a certain threshold.

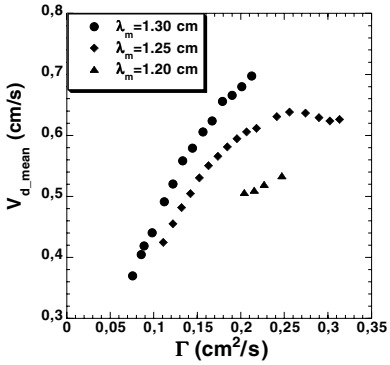

(a)

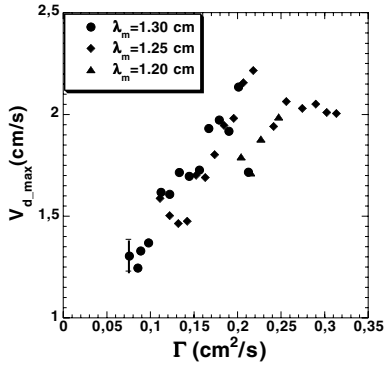

(b)

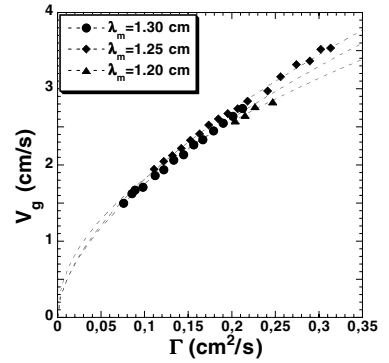

(c)

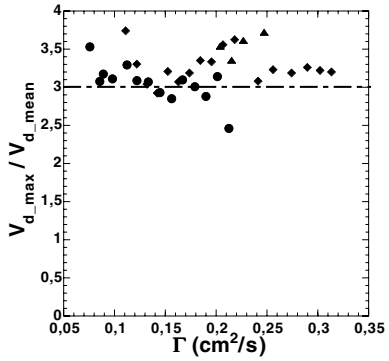

(d)

Fig. 27. Velocity measurements of an oscillating-drifting state, for different number of columns (η = 200 cP, d = 10 cm). (a) Mean phase speed. (b) Maximal phase speed. (c) Group velocity. (d) Ratio V_{dmax}/V_{dmoy}.

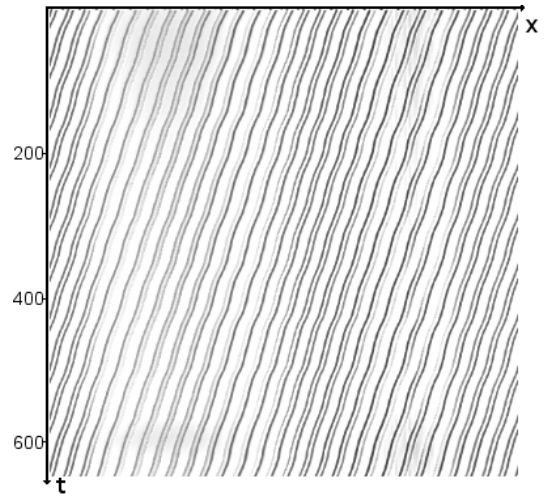

(a)

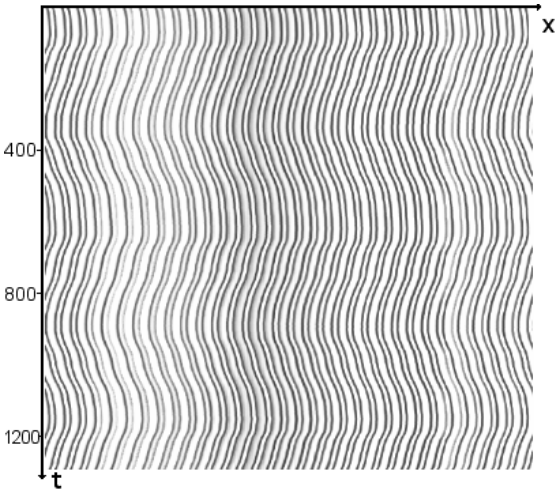

(b)

Fig. 28. Diagrams of slow-drift states (η = 200 cP, d = 10 cm). (a) Γ = 0.089 cm^2/s, 28 cols. (λ = 1.067 cm). Duration 640 s. (b) Slow drift with several changes of direction (Γ = 0.266 cm^2/s, 32 cols. λ = 0.933 cm. Duration 1280 s).

The direction of the slow drift is chosen by the system: presumably, this direction is fixed by imperfections of initial conditions, i.e. by initial tiny departures from spatial homogeneity. Furthermore, in most conditions, the system keeps the initially chosen direction. An example is depicted in Figure 28a. It is remarkable that slow undulations are superimposed to the drift. We have observed that at lower flow-rates, these undulations can exist without any drift.

The range of Γ for the existence of these states is also bounded by a upper threshold. Above the threshold, they cease to exist and transit to other dynamical states, see stability diagrams Figures 8 to 10. Close to this upper limit, the drift can spontaneously changes its direction, as shown in Figure 28b. These unstable phenomena occur

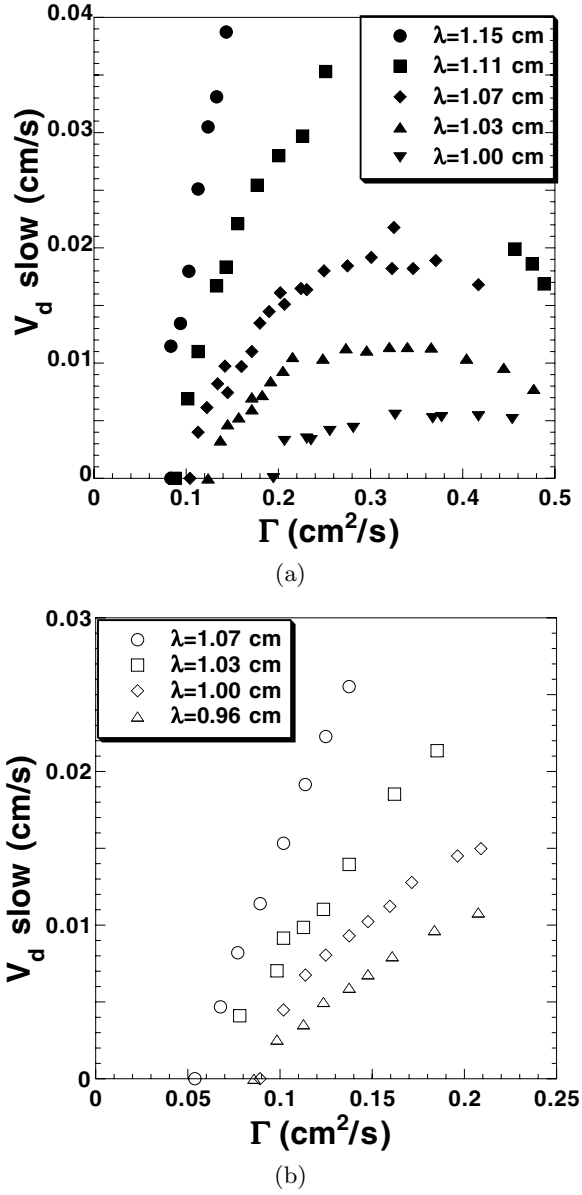

Fig. 29. Measurements of the slow-drift velocity versus flow-rate, for different λ ($d = 10$ cm). (a) $\eta = 100$ cP. (b) $\eta = 200$ cP.

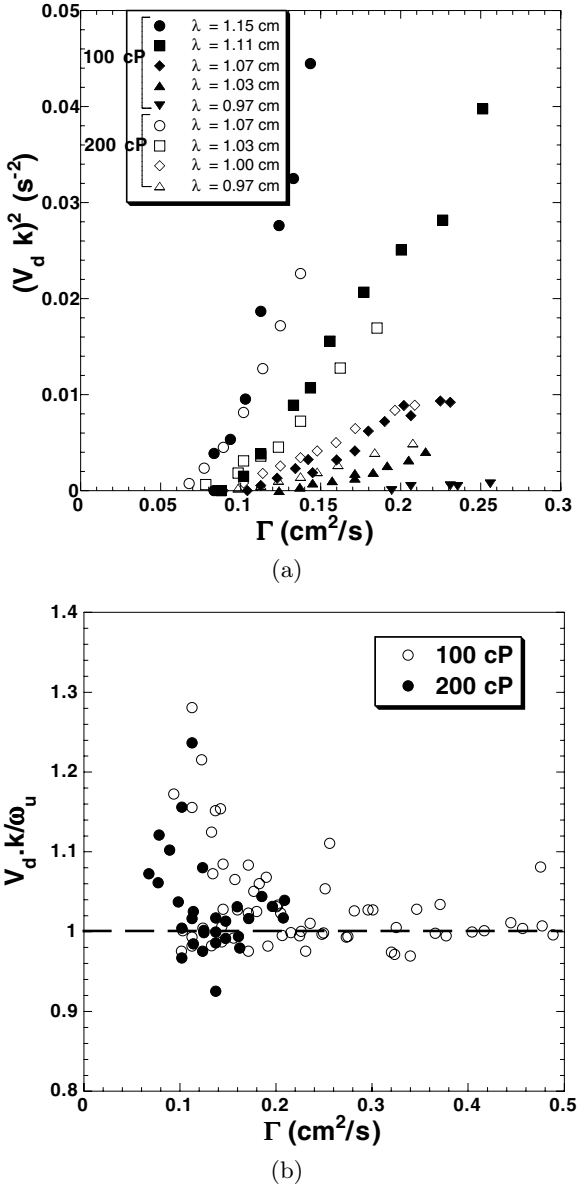

Fig. 30. (a) $(V_d k)^2$ versus flow-rate, for two viscosities 100 cP (black symbols) and 200 cP (open symbols). (b) The dimensionless quantity $(V_d k)/\omega_u$ versus flow-rate.

in a narrow range of parameters, and perhaps constitute the first step to the destabilization towards OSC or STC regimes at increasing flow-rate.

The quantitative study of such a regime needs long acquisitions (up to 20 min), and then requires a much longer time step between each line of spatiotemporal diagrams than for usual dynamical regimes. Measurements of the drift velocity V_{dslow} are reported in Figures 29a et 29b for two viscosities 100 and 200 cP.

The velocity is an increasing function of λ, and η, as does the drift velocity of LD and GD states. Otherwise, the minimal flow-rate threshold to trigger the slow-drift, namely Γ_{cs}, decreases at higher λ_m and higher η.

If one analyses the data more carefully, it turns out that the velocity follows a square-root law with the flow-rate, just as the LD and GD states. Figure 30a plots the quantity $(V_d k)^2$ versus Γ, for values close to threshold. These results suggest that the bifurcation to a slow drift is supercritical. In order to build a dispersion relation between slow drift and undulations, the quantity $V_d k$ is then compared to the measured pulsation of undulations ω_u. It turns out that the ratio $V_d k/\omega_u$ is close to one when the flow-rate is high enough.

To summarize, the slow drift velocity obeys the simple empirical relationship:

$$(V_d k)^2 = \alpha_s(\Gamma - \Gamma_{cs}) \tag{18}$$

with α_s and Γ_{cs} which are functions of λ and η.

It is remarkable that the slow drift and the 'usual' drift due to parity-breaking of cells, show up striking similarities in their relation $V_d(\Gamma)$, see equations (11) and (18), although the velocities differ by two orders of magnitude, and keeping in mind that these two states originate from distinct mechanisms. Consequently, it would be interesting to approach this state with amplitude/phase equations, similarly to Goldstein et al. model [36]. The difficulty is here to identify an equivalent of the cell asymmetry: with the visualization accuracy we were able to achieve, no apparent asymmetry could be noticed during the slow drift.

Such slow dynamical phenomena have also been observed in the printer's instability [9] in the form of slow in-phase oscillations of cells, then rather like the situation of Figure 28b. Otherwise in the printer's instability, slow motions stop after some hours [9], which was not noticed on the pattern of columns: they could here be recorded during more than one day, before the acquisition was stopped.

There are still some points that remain to be clarified. Amongst them, it is unclear why this state appears above a certain threshold. What determines this threshold value? Why does spontaneous changes of direction occur?

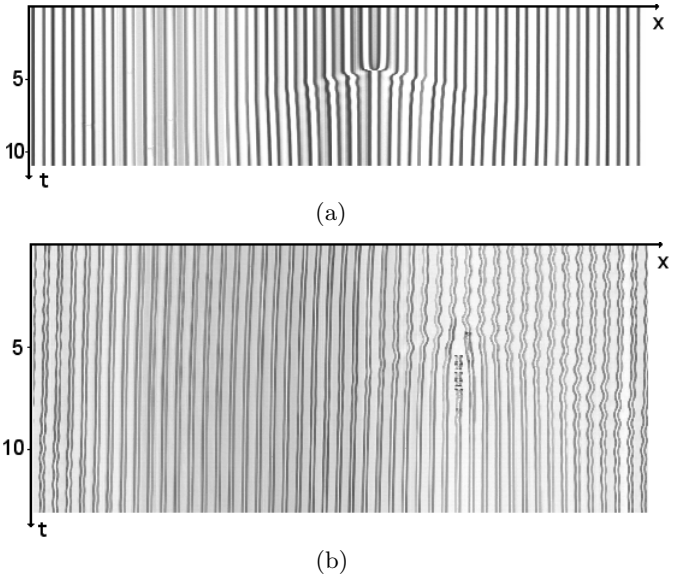

Fig. 31. (a) Two merging columns after an increase of flow-rate: $\eta = 100$ cP, $d = 10$ cm, $\Gamma = 0.45$ cm^2/s, $N = 32$ and finally 31 columns. (b) Column nucleation after transient oscillations: $\eta = 100$ cP, $d = 16.7$ cm, $\Gamma = 0.16$ cm^2/s, $N = 45$ and finally 46 columns.

6 The breakup of dynamical states

In this section, we relate a catalogue of different break-up scenarios of ordered regimes. Such situations are generally triggered after the flow-rate be progressively increased or decreased, in order to cross the boundaries of stability domains described in Figures 8–10.

Starting from initial conditions at given flow-rate and number/positions of columns, one lets the system evolve and converge to an asymptotic state. In a second step, the flow-rate is varied and we observe how the pattern evolves. The break-up of the initial state is often associated to occurrences of one or several defects, i.e. changes in the number of columns. However, this is not always the case: a change of state can sometimes be observed without any defect occurrences. Anyway, the resulting final state can either be a laminar regime distinct from the initial one, or a chaotic one.

6.1 Break-up of static and quasi-static states

A static regime can break through various scenarios. The transition to dripping occurs when the flow-rate per column is lowered under a threshold value: $q \leq q_c$, with $q = Q/N$. For some values of λ_m, an increase of flow-rate can lead to a slow-drift superimposed to slow undulations, as shown in Figures 28. In most cases, the slow-drift is the first stage towards more dramatic transitions: if the flow-rate is increased further, the pattern will show oscillations, propagative domains or chaos. However, it is difficult to figure out how the slow dynamics interacts with the other swift regimes and eventually influence the break-up scenarios. As previously shown, it could be for instance related to the localization of oscillations (Fig. 16).

To summarize, by increasing flow-rate Γ above a certain threshold, from an initial static or quasi-static state, two following break-up scenarios are observed:

- For $\lambda \simeq \lambda_{min}$ or slightly larger (shrunk structure), an increase of flow-rate can lead to the merging of two columns into a single one. This leads to an increase of λ_m, see Figure 31a. This secondary instability is seemingly an Eckhaus instability, followed by an adjustment due to phase-diffusion. The subsequent motions of columns are more significant in the vicinity of the defect. The Eckhaus instability itself is provoked by phase inhomogeneities in the initial pattern. This instability is ubiquitous in other similar systems, like the printer's instability [8], the directional solidification [13,15] and the KS equation [21].
- For $\lambda > \lambda_0$, a change of Γ can trigger an oscillatory state (the change is generally an increase of Γ, but it can be a decrease in the case $\eta = 20$ cP). In a further stage, a defect (birth of a column) appears and then the system reaches a new stable state (Fig. 31b). In some situations, it was even observed that the system could directly turn to a LD or a STC state, after a short oscillatory transient.

6.2 Break-up of drifting states

Within the denomination 'drifting states', are included both LD and GD. We first report break-up of GD states

when the lower limit of Γ if crossed. In that situation, two main scenarios are observed:

- the break-up can be caused by the rupture of one or several columns that turn into dripping sites. Generally, the dripping site does not follow the drift motion of columns, which provokes a cascade of subsequent break-ups to consecutive sites (Fig. 32a). This transition to dripping originates from the Rayleigh instability, that causes the pinch-off of a column at its top for low enough flow-rate. As for static states, the break-up occurs below a threshold flow-rate per column q_c. The value of q_c is 0.07 cm^3/s for the 100 cP oil;
- the break-up can be caused by a phase-instability, witnessed by oscillations of the positions of columns prior to break-up (Fig. 32b). This scenario arises for q higher than q_c and concerns the most dilated GD states (obtained with λ_m larger than 1.9 cm for the 100 cP oil). At the ending stage, the Rayleigh instability also occurs. This phase instability shows that the parity-breaking mode involved in GD and LD is unstable near the threshold value of $\mu + \epsilon\phi_x$ (recalling that μ is identifiable to $(\Gamma - \Gamma_c)$, see equations (4) and (14), as it was predicted by usual models [37,39].

Figure 32 also illustrates a fact that was briefly invoked at the end of Section 4.1, i.e. that dripping sites cannot move along x: as soon as a column turns into a dripping site, its motion — previously a drifting one — vanishes.

When the upper flow-rate limit is reached, it is observed that the rupture of a drifting state can result either to another drifting state with a larger number of columns, either to a static state, either to a chaotic state. The latter situation is only encountered for a high enough viscosity (100 or 200 cP). Figures 33a to c give several examples of break-ups of GD states, and Figures 34a to c show some examples of broken LD states.

Amongst this host of break-up scenarios, some phenomena deserve further comments:

- Oscillations of drifting columns, appearing near both lower (Fig. 32b) and upper (Fig. 33b) thresholds, are of the same nature. This oscillatory behavior, which is the first stage of the rupture of GD states, does not have to be confused with the oscillating-drifting state (OSD) shown in Figure 6, which rather consists in successive small propagative domains. After careful observations, it is noticeable that between each pair of columns, an intermediate drop (the one that initially breaks the parity symmetry of the arch) shows periodic cycles of growth and retraction. A part of the liquid in this drop is periodically absorbed by one of the columns, so that its growth is hindered like in the period-doubling oscillatory states. Then it grows again. This cycle of growth and absorption has a well-defined characteristic time, of the order of one second. From a point of view of a phase instability, the growth of such transient drop may signify that, in this range of parameters, the system tries to catch a smaller wavelength than the one imposed initially.
- A global drifting state generally gets unstable beyond a critical flow-rate, that is higher than the upper limit for local drifting states, see also Figure 21. To explain this fact, we propose the following: the break-up of local domains is generally initiated in the oscillating wake, the period-doubling oscillations being much less stable at high flow-rate. Then the first defect occurrence that triggers break-up, is observed in the bulk of the wake. This is an important mechanism for the creation of disorder [25,26]. Then, because they do not contain such an oscillating wake, GD states can be withstood at flow-rate higher than LD states.

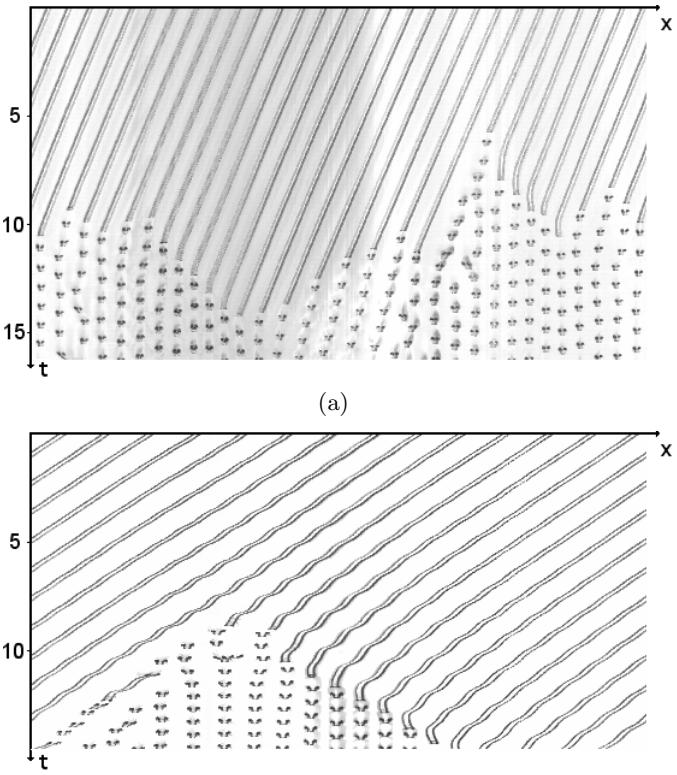

Fig. 32. Break-up of drifting states, when decreasing flow-rate, $\eta = 100$ cP. (a) Pinch-off of a column into drops, and cascade of generations of dripping sites: $d = 16.7$ cm, $N = 29$, $\Gamma = 0.042$ cm^2/s. (b) Oscillatory instability as a first stage to break-up, with final dripping sites: $d = 10$ cm, $N = 14$, $\Gamma = 0.055$ cm^2/s.

6.3 Break-up of oscillatory states

Extended oscillatory regimes appear in a reduced range of parameters for all the viscosities we used. Their stability is then particularly sensitive to any variation of flow-rate. When Γ is decreased, starting from an oscillatory regime, one observes that oscillations progressively fade out and that the pattern turns static. This transition occurs without any defect. A similar scenario is also observed when one increases Γ at low-viscosity (20 cP). However, at higher viscosities (50 to 200 cP), the increase of Γ leads to a different behavior: it generally breaks the state with the generation of defects. At 50 cP, the final state is either S or LD; but at 100 or 200 cP, the final state is LD

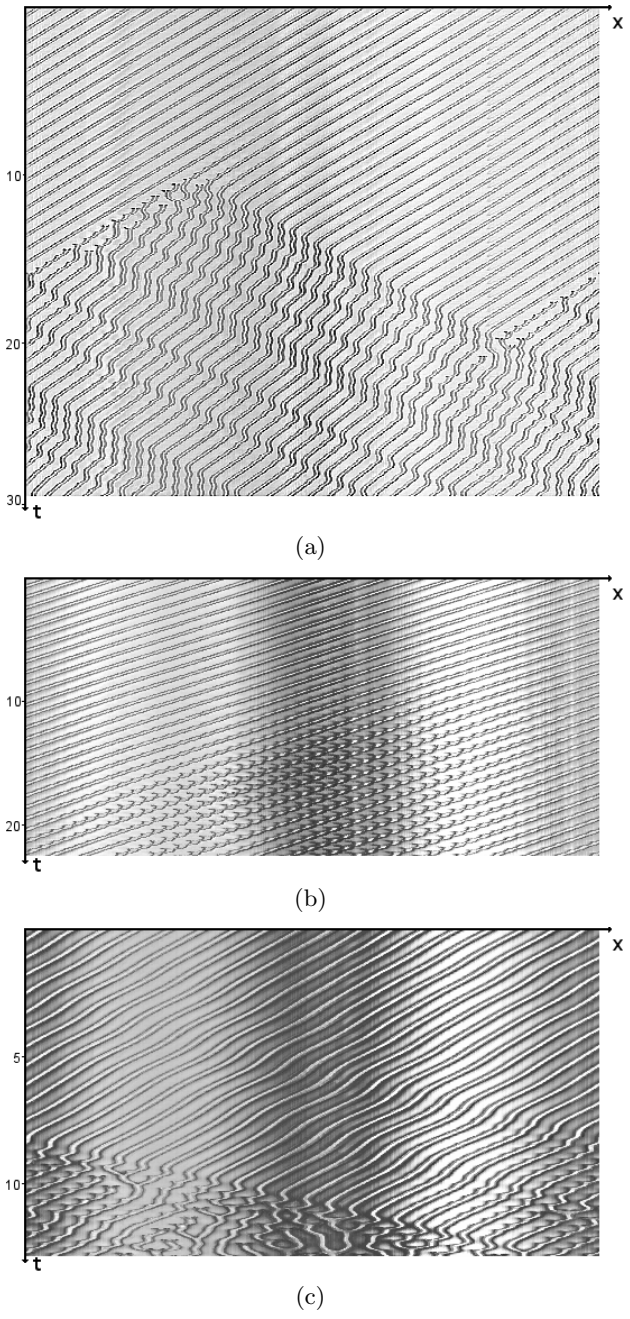

Fig. 33. Examples of break-up of global drifting states approaching the upper flow-rate limit (η = 100 cP). (a) Final state: several domains following each other (d = 16.7 cm, N = 25, Γ = 0.28 cm^2/s). (b) Oscillations as first step of destabilization: d = 10 cm, N = 17, Γ = 0.36 cm^2/s. (c) Transition towards spatiotemporal chaos: d = 10 cm, N = 17, Γ = 0.55 cm^2/s.

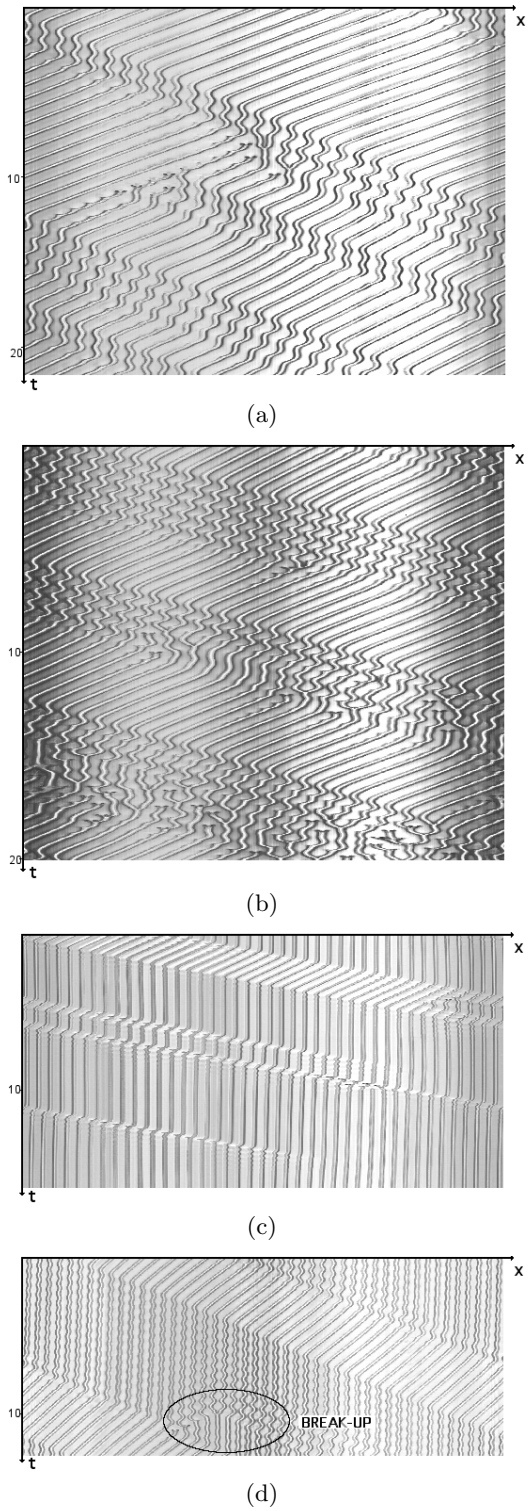

Fig. 34. Examples of break-up of propagative domains approaching the upper flow-rate limit, η = 100 cP except (c). (a) The final state consists in multiple domains: d = 10 cm, N = 16, Γ = 0.176 cm^2/s. (b) Transition towards spatiotemporal chaos: d = 10 cm, N = 21, Γ = 0.5 cm^2/s. (c) Transition to a static state: η = 20 cP, d = 16.7 cm, N = 37, Γ = 0.32 cm^2/s. (d) Break-up induced by amplification of oscillations following the trailing-edge of the domain: d = 16.7 cm, N = 41, Γ = 0.33 cm^2/s.

(Fig. 35a) or STC (Fig. 35b). Seldom, a LD is created without any defect (Fig. 35c).

Thus, the three presented situations emphasize the non-trivial interactions between oscillations and propagative domains: it was previously shown in Figures 5a and 34d that out-of-phase oscillations follow propagative domains. Figures 35a to 35c show in some sense the inverse

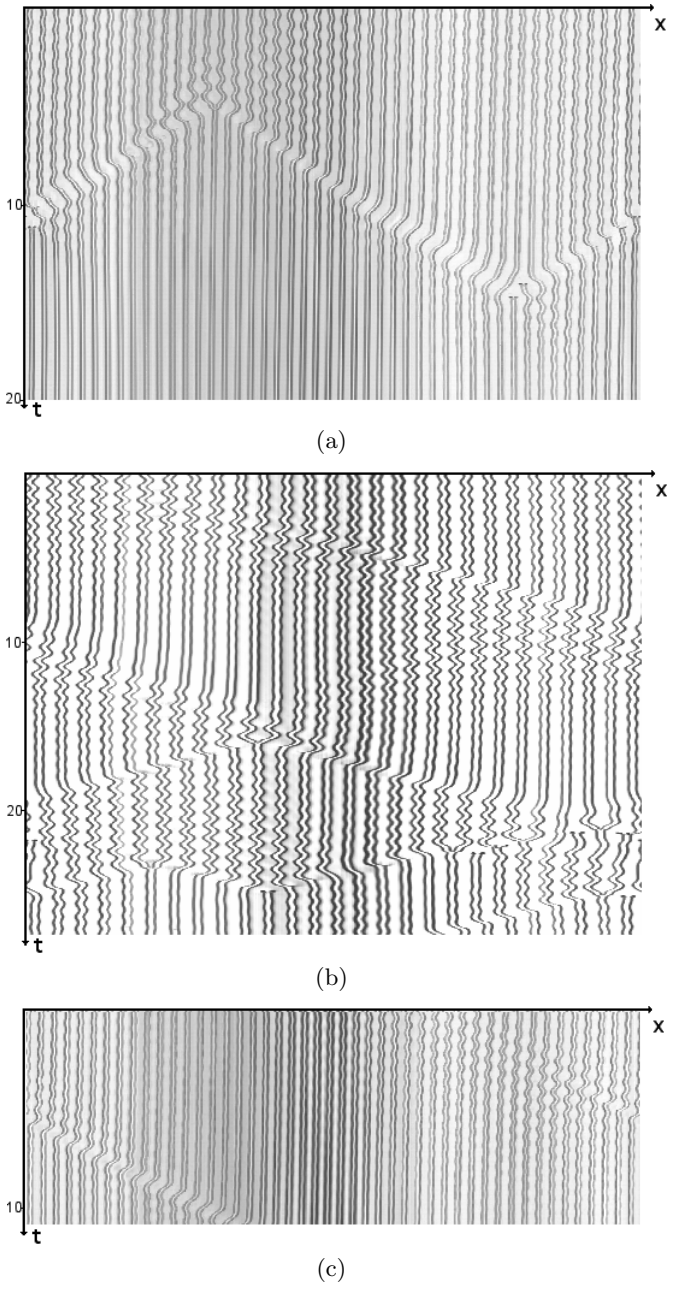

Fig. 35. Break-up of an oscillatory state induced by an increase of flow-rate ($\eta = 100$ cP). (a) A pair of domains propagating to opposite directions are generated by the break-up ($d = 16.7$ cm, $N = 46$, $\Gamma = 0.27$ cm^2/s). (b) Transition towards spatiotemporal chaos ($d = 10$ cm, $N = 27$, $\Gamma = 0.29$ cm^2/s). (c) A domain is created although no defect is shown ($d = 16.7$ cm, $N = 45$, $\Gamma = 0.225$ cm^2/s).

process: oscillations can lead to small propagative domains when they get amplified enough.

6.4 Collision between two propagative domains

In this paragraph, we relate seemingly marginal situations, although they are spectacular and tell about how propagative structures get involved in the production of disorder. These situations consist of two propagating domains, that travel in opposite directions and collide with each other after a short while. For these experiments, the largest dish ($d = 16.7$ cm) has been used, in order to enable the development of two independent domains. To set up such a situation, one launches the two domains close to each other, using the method described in the experimental set-up.

Figures 36 show three examples of collisions: (a) two domains with same size cancel each other when they collide. If one of the domains is larger than the other one, it will continue its course, but its size is decreased by the size of the smaller one (b and c).

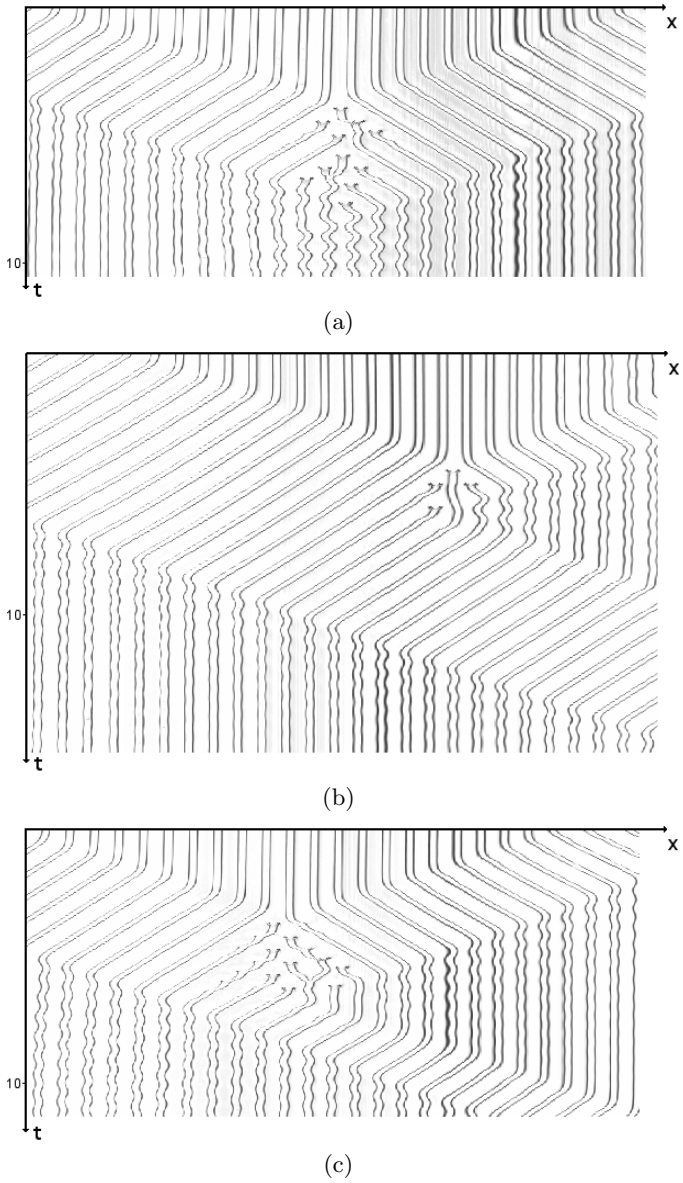

Fig. 36. Collisions between two domains propagating to opposite directions ($\eta = 100$ cP, $\Gamma = 0.276$ cm^2/s). (a) Same size for the two domains: cancelation of drift and transient oscillations. (b) and (c) Different sizes: only the largest one survives, with a final smaller size.

It is worth noticing that such a behavior has been observed in experiments of directional solidification [12] and in the Goldstein et al. model [36].

Several features can be extracted from such observations. First, although these domains are often referred as 'solitary waves' in the literature, they can not be qualified as solitons, the collisions of which are not destructive. Second, generated defects during collisions of propagating domains are involved in the process of disorder creation [26]. In that sense, propagative domains indirectly contribute to chaos, even though they are perfectly predictable.

7 Conclusion

The study reported in this paper has been focused on the ordered dynamics of the pattern of columns, through three main points. (1) A broad view of the different regimes has been presented, with the overall pictures of their range of stability, for different viscosities. (2) Exhaustive measurements have shown the general tendencies of oscillating and drifting states, varying η, Γ and λ in the maximal allowed ranges. The extended range of stability for dynamical regimes at high viscosities is an asset for such a quantitative study, and to our knowledge, our system is the only one that can enable this. (3) A host of break-up scenarios of various regimes has been presented. They show transitions from a well-defined laminar state to an another one, as well as different routes to spatio-temporal chaos. Most of these transitions are accompanied with defects.

Amongst the results gathered in this study, some conclusive points of more general interest can be drawn.

– The pattern of liquid columns exhibits a host of states, particularly at higher viscosities where the richest dynamics is observed, with a large range of existence for the regime of spatio-temporal chaos. Also, a complex but predictable oscillating-drifting state, which owns the striking property of spatial tri-periodicity, has been evidenced. To our knowledge, no available model or set of equations dedicated on one-dimensional patterns could reproduce such a state.

– A generic set of equations has been found to describe regimes of parity-broken drifting cells. Especially, checking the dependency on λ has revealed relationships between the phase and group velocities on one side, and the local phase gradients on the other side. This has enabled an accurate determination of coefficients for this system in the initial model by Goldstein et al. [36], and has emphasized the need for adding higher order terms. A rescaling, based on this modified model, has revealed that both localized and global states obey the same kinetics.

– Although originating from distinct mechanisms, the regime of slow drift and the regime of parity-broken drifting cells have several features in common: the drifting speed of the cells increases with λ, Γ and η in both regimes. Also, their appearance needs that Γ overcomes a certain threshold, that is wavelength-dependent. Many remaining questions concern the regime of slow drift: particularly how a process of phase diffusion can spontaneously trigger a homogeneous displacement of the columns.

– Many features of the array of columns show similarities with other pattern forming unstable fronts. Considering morphology and space/time scales, the most resembling experimental system should be the directional viscous fingering [6–11]. Otherwise, some situations of directional solidification with lamellar eutectics [15], although dealing with smaller space- and longer time-scales, have shown striking similarities with our system, particularly on the further destabilization of bifurcated states: amplitude holes within an oscillating period-doubling state, oscillations of global drifting states (denoted as $T - x\lambda O$ in [15]) or a pair of propagating 'tilted' domains launched at the break-up of an oscillating patch [14]. All these systems are suitable to provide inputs in order to validate and improve existing models. As an alternative approach, some attempts to calculate the secondary instabilities of the KS equation, from an initial cellular solution with a few tens of cells, have reproduced several typical behaviors resulting from non-trivial mode interactions: for instance, oscillating wakes behind propagative domains, phase jumps and amplitude holes in oscillating regimes, or oscillations prior to ruptures of global drifting states [58]. Thus we believe that such an equation is likely to capture many other behavior of that class of systems, and could constitute a powerful predictive tool. Still there are no obvious direct identifications between control parameters of experiments and coefficients of the KS equation.

Appendix A: Static states: liquid thickness and lubrication theory

Let us first present simple arguments predicting h, the thickness of liquid let below the overhang for a static state. Considering Figure A.1a, we define q as the flow-rate through each column and we obtain: $q = \Gamma\lambda$. Defining r as the radial coordinate from the center of a column, it is possible to write a relationship that gives a coarse value for the radial flow around a column: $hu_r \simeq q/2\pi r$, u_r being the radial speed. The latter relationship traduces that the gravity drainage between each column (q) leads to a radial, horizontal flow.

Let us first reduce to a 2D problem in the plane of the figure and then identify u_r to u_x, the mean velocity along the x axis. Close to the saddle point $x = 0$ ($r = \lambda/2$), we have the superimposition of two flows along x:

$$hu_x = \frac{\Gamma\lambda}{2\pi(\lambda/2 - x)} - \frac{\Gamma\lambda}{2\pi(\lambda/2 + x)}.$$

Then for x close to 0, one obtains:

$$h_0 u_x = \frac{4}{\pi}\frac{\Gamma x}{\lambda}. \tag{19}$$

In order to find a relationship for the speed u_x, we naturally write an equilibrium between gravity and viscous

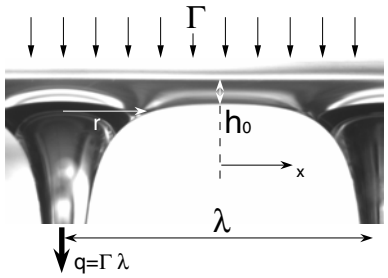

(a)

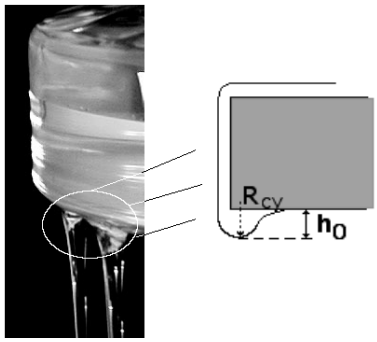

(b)

Fig. A.1. (a) Sketch of the flow around a column. (b) Side view of the arch between two columns.

forces, under the assumption of the lubrication theory:

$$\boldsymbol{u} = -\frac{h^2}{3\eta}\boldsymbol{\nabla} P.$$

Taking the pressure P as $-\rho g h$, or $P = -\rho g x^2/2R_{cx}$ close to the saddle point ($x \ll \lambda$), we obtain:

$$u_x \simeq \frac{\rho g h_0^2}{3\eta}\frac{x}{R_{cx}}$$

R_{cx} being the radius of curvature of the interface at the saddle point of the arch, in the plane of the figure. We straightforwardly identify this relationship to equation (19):

$$h_0^3 \simeq \frac{3\eta}{\rho g}\Gamma\frac{R_{cx}}{\lambda}. \tag{20}$$

A naive but natural choice for R_{cx} would be a value of the order of the characteristic length in the x direction: $R_{cx} \sim \lambda/2$, which would lead to:

$$h_0^3 \simeq \frac{6\eta}{\rho g}\Gamma. \tag{21}$$

This is the tendency given by the lubrication theory.

We confront the above simple ideas with measurements of the film thickness between two columns in a static state, at the saddle point of the arch h_0. This corresponds to a local minimal thickness of liquid that coats the overhang. Figure A.2-a shows h_0 for $\eta = 100$ cP versus Γ, for various wavelengths λ. Similar results have been obtained using different viscosities. It is shown that the data are correctly fitted by square-roots laws. The following empirical relation provides a good approximation of the thickness:

$$h_0 \sim f(\lambda, \eta)\Gamma^{1/2} \tag{22}$$

with f being an increasing function of λ and η.

The thickness h_0 follows a different behavior from what is predicted by the lubrication theory. The latter predicts an evolution of h_0 as the power one-third of Γ and no dependency on λ (see Eqs. (20) and (21)). Instead, h_0 increases like the square-root of flow-rate, and increases for larger λ. The influence of viscosity has been explored: with a viscosity twice larger ($\eta = 200$ cP) the thickness is measured 1.2 to 1.5 times larger for the same Γ and λ.

This behavior suggest that the naive arguments leading to equation (21) should be flawed. First, R_{cx} may show a more subtle dependency on λ (as it will be shown later). Otherwise, it was observed that the transverse radius of curvature R_{cy} should be of order of the thickness h and then much smaller than R_{cx} (see Fig. A.1). Thus, the dominant curvature should be $R_{cy}^{-1} \simeq h^{-1}$, and it suggests that this strong local curvature could lead to an internal pressure in the film below the overhang: $P \sim \gamma/R_{cy} \sim \gamma/h$.

Thus, replacing $P = -\rho g z$ by $P = \gamma/h$ in the lubrication theory, one obtains:

$$u_x \simeq -\frac{h^2}{3\eta}\partial_x\left(\frac{\gamma}{h}\right) \simeq \frac{\gamma}{3\eta}\partial_x h.$$

Then, after a multiplication by h_0 and assuming a parabolic shape close to the saddle point: $h = h_0\left(1 + \frac{x^2}{l_x^2}\right)$:

$$h_0 u_x \simeq \frac{2\gamma h_0^2}{3\eta l_x^2}x.$$

Let us note that l_x and R_{cx} are linked by: $R_{cx} = \frac{l_x^2}{2h_0}$. If we identify to (19), we finally obtains:

$$h_0 = \left(\frac{6\eta}{\pi\gamma}\frac{l_x^2}{\lambda}\right)^{1/2}\Gamma^{1/2}. \tag{23}$$

Therefore, taking the assumption that the pressure in the liquid layer is governed by capillary effects, and assuming that the layer takes the shape of a 'tube' of slowly varying diameter in the vicinity of the saddle point, we find an expression for h_0 consistent with measurements (at least at this stage, for the dependency on Γ). The length l_x representing the parameter of the parabolic fit of the arch close to the saddle point contains an implicit dependency on λ. In order to find a reliable expression for l_x, we check this dependency.

Figure A.2b proposes that plotting the quantity $h_0^2/(\lambda - \lambda_s)$ versus flow-rate makes the data collapse on the same linear curve, taking $\lambda_s = 0.75$ cm. It leads to an expression for l_x that reads: $l_x^2 \sim \lambda \times (\lambda - \lambda_s)$. Other possible choice for the dependency of h_0 with λ have also been found to make the data collapse (for example by plotting $h_0^2\lambda^{-3/2}$), but the one we kept, offers suitable order of magnitude and variations for l_x: this last point was checked by directly extracting l_x from parabolic fits of the

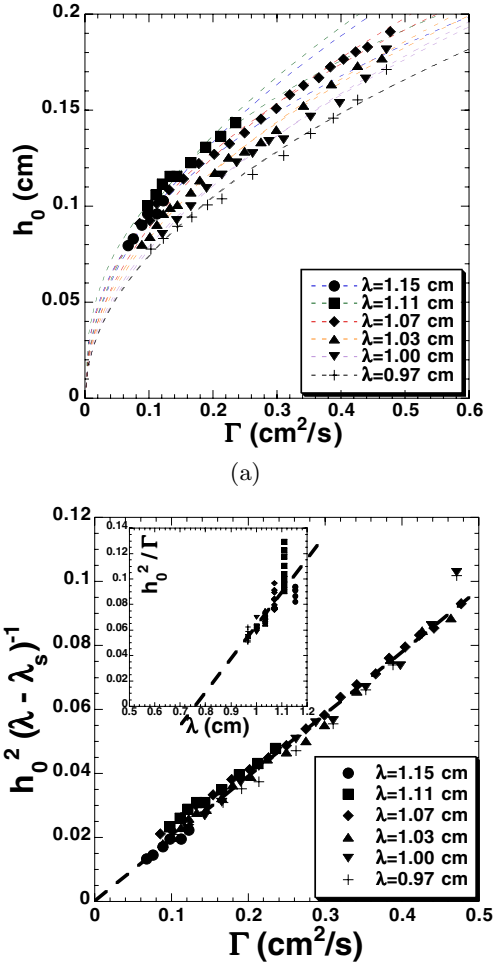

Fig. A.2. (a) Liquid thickness between two columns, at the saddle point of an arch h_0 ($\eta = 100$ cP). Dashed lines stand for square-root laws that provided the best fit. (b) The plot of the quantity $h_0^2(\lambda - \lambda_s)^{-1}$ versus flow-rate collapses points on a single linear curve. Insert: the plot h_0^2/Γ that has suggested the rescalling.

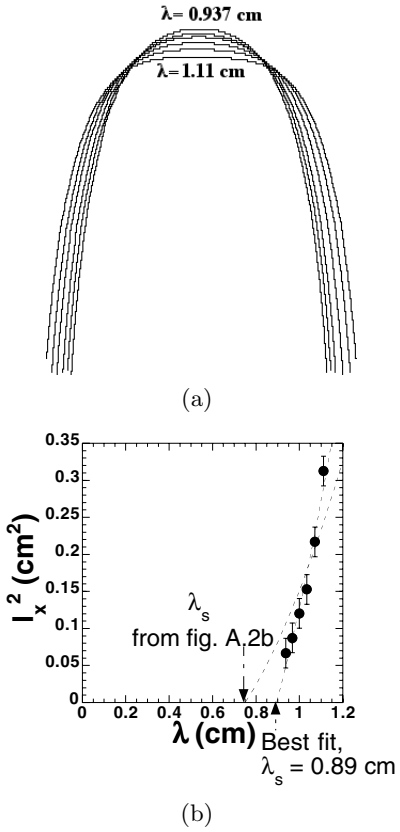

Fig. A.3. (a) Extraction of the shapes of arches at different wavelengths, for the same flow-rate $\Gamma = 0.177$ cm^2/s. (b) The length l_x, characterizing the shape of arches, versus λ. ($\eta = 100$ cP).

shapes in the vicinity of the saddle point. The results are illustrated in Figure A.3, on which the measured values of l_x are plotted versus λ. It indeed appears that l_x converges to zero at a finite value of λ, which suggests the expression given above. However the agreement is only qualitative as the value for the offset λ_s is close to 0.89 cm instead of the value of 0.75 cm found for the best plot of $h_0^2/(\lambda - \lambda_s)$ (with a pre-factor close to one). It is also not excluded that λ_s could slightly depend on flow-rate, despite the master curve of Figure A.2b used a fixed value for λ_s. The empirical law that is kept for h_0 is the one obtained from the master curve of Figure A.2b:

$$h_0 \simeq \left(\frac{6\eta}{\pi\gamma}\right)^{1/2} (\lambda - \lambda_s)^{1/2} \Gamma^{1/2} \qquad (24)$$

with $\lambda_s = 0.75$ cm.

Of course, this description is still incomplete, but it gives a meaningful idea of the hydrodynamics of static columns.

Appendix B: coarse prediction for the pulsation of oscillations from thickness measurements

On Figure B.1 are defined the different quantities on interest. This scheme is supported by direct observations of a transiently (and periodically) growing drop between two oscillating columns, when the spacing between them is maximal (see also [33]). If one tries to roughly evaluate the volume of such a transient drop, one obtains $V = \lambda h_0 2\pi l_c$, multiplying the three characteristic lengths along the azimuthal (λ), the vertical (h_0) and the radial direction ($2\pi l_c$), recalling that l_c is the capillary length equal to $\sqrt{\gamma/\rho g}$. Between two columns, the injected quantity of liquid is $\Gamma\lambda$. The characteristic time, necessary to fill a transient drop is:

$$\tau_R \simeq \frac{2\pi l_c \lambda h_0}{\Gamma\lambda}$$

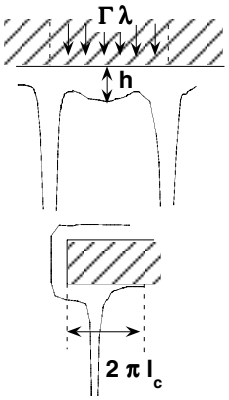

Fig. B.1. Sketch of the dimensional argument, leading to equation (26).

which evaluates the angular frequency to:

$$\omega \simeq \frac{\Gamma}{l_c h_0}.$$

Considering values of h_0 that are presented in the previous Appendix, the order of magnitude for ω is found around 10 rad/s, which is close to the experimentally found values, see Figure 13a. The obtained values for C, from the fit of ω versus Γ, are plotted on Figure 13b. They suggest that a higher viscosity coarsely leads to a decrease of ω as a power law with an exponent between 0.1 and 0.2. In the previous Appendix, the fit of experimental data has led to equation (24) for h_0. Thus, a simplified law for ω can be proposed:

$$\omega \simeq \left(\frac{\pi\gamma}{6\eta l_c^2}\right)^{1/2} (\lambda - \lambda_s)^{-1/2} \Gamma^{1/2}, \qquad (25)$$

$$\simeq \left(\frac{\pi\rho g}{6\eta}\right)^{1/2} (\lambda - \lambda_s)^{-1/2} \Gamma^{1/2}. \qquad (26)$$

The relationship between ω and the viscosity does not simply come up. From equation (26) and the definition of C, we can state that:

$$C \simeq (\pi\rho g/6)^{1/2} (\lambda - \lambda_s)^{-1/2} \eta^{-1/2}. \qquad (27)$$

Measurements of oscillating regimes are performed with a wavelength λ very close to λ_0, so that we can take it as the value for λ. The variation of λ_0 with viscosity is shown in Figure 12. Plotting the value for C obtained from the fit of $\omega/\Gamma^{1/2}$ versus the expression given above, one obtains the plot of Figure B.2. The qualitative tendency is satisfactory although a departure from a linear relationship is noticed. The length λ_s was also assumed not to depend on η, which could be a cause for the departure. Thus, equation (27) provides a tentative scaling for the value of C, in agreement with both direct measurements of ω and phenomenological approaches based of measurements of h_0. The latter are based on the argument that the pulsation of oscillations is linked to the time for turning the liquid film of an arch into a pendant drop between two columns.

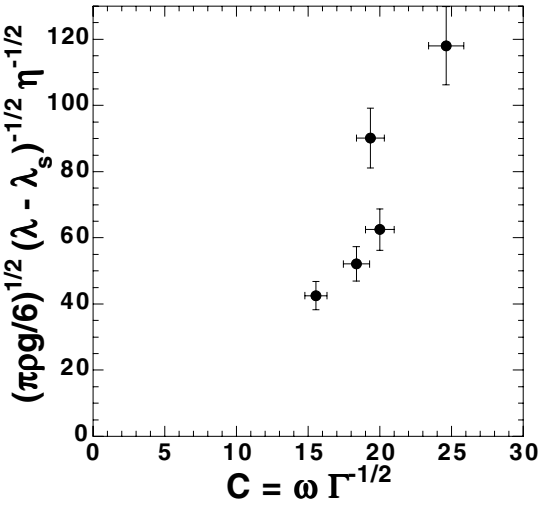

Fig. B.2. Check of the variation of C with viscosity.

To summarize, semi-empirical arguments provide rather convincing results, despite a complete quantitative agreement could not be brought up. Consequently to dynamics ruled by the complex free surface below the overhang, simple hydrodynamical arguments show their limitation for a complete description of phenomena. Otherwise, a more precise description of these regimes can benefit from more phenomenological approaches [7,25,33]. These approaches were inspired from that oscillations and drifts seemingly originate from a common mechanism. The occurrence of an oscillating wake left behind a propagative domain constitutes an illustration of this statement.

References

1. M.C. Cross, P.C. Hohenberg, Rev. Mod. Phys. **65**, 851 (1993)
2. M.I. Rabinovich, A.B. Ezersky, P.D. Weidman, *The dynamics of patterns* (World Scientific Publishing, 1998)
3. A. Prigent et al., Phys. Rev. Lett. **89** 014501 (2002)
4. D. Barkley, L.S. Tukerman, Phys. Rev. Lett. **94**, 014502 (2005)
5. R. Kerswell, Nonlinearity **18**, R17R44 (2005)
6. M. Rabaud, S. Michalland, Y. Couder, Phys. Rev. Lett. **64**, 184 (1990)
7. S. Michalland, M. Rabaud, Physica D **61**, 197 (1992)
8. H. Cummins, L. Fourtune, M. Rabaud, Phys. Rev. E **47**, 1727 (1993)
9. L. Fourtune, W.J. Rappel, M. Rabaud, Phys. Rev. E **49**, R3576 (1994)
10. L. Pan, J.R. de Bruyn, Phys. Rev. Lett. **70**, 1791 (1993)
11. L. Pan, J.R. de Bruyn, Phys. Rev. E **49**, 483 (1994)
12. A.J. Simon, J. Bechhoefer, A. Libchaber, Phys. Rev. Lett. **61**, 2574 (1988)
13. J.-M. Flesselles, A.J. Simon, A.J. Libchaber, Adv. Phys. **40**, 1 (1991)
14. G. Faivre, J. Mergy, Phys. Rev. A **46** 963 (1992)
15. M. Ginibre, S. Akamatsu, G. Faivre, Phys. Rev. E **56** 780 (1997)
16. P. Rupp, R. Richter, I. Rehberg, Phys. Rev. E **67**, 036209 (2003)

17. J. Burguete, D. Maza, H.L. Mancini, Physica D **174**, 56 (2003)
18. Y. Kuramoto, *Chemical oscillations, waves and turbulence* (Springer-Verlag, 1978)
19. A. Pumir, P. Manneville, Y. Pomeau, J. Fluid Mech. **135** 27 (1983)
20. P. Manneville, *The Kuramoto-Sivashinsky equation: a progress report*, in *Propagation in systems far from equilibrium* (Springer Verlag, 1991)
21. C. Misbah, A. Valance, Phys. Rev. E **49**, 166 (1994)
22. C. Counillon, L. Daudet, T. Podgorski, M.C. Jullien, S. Akamatsu, L. Limat, Europhys. Lett. **40**, 37 (1997)
23. C. Counillon, L. Daudet, T. Podgorski, L. Limat, Phys. Rev. Lett. **80**, 2117 (1998)
24. P. Brunet, J.-M. Flesselles, L. Limat, Europhys. Lett. **56**, 221 (2001)
25. P. Brunet, J.-M. Flesselles, L. Limat, Eur. Phys. J. B **35**, 525 (2003)
26. P. Brunet, L. Limat, Phys. Rev. E **70**, 046207 (2004)
27. Lord Rayleigh, *Scientific papers* (Cambridge University Press, Oxford, 1900), Vol. II
28. G.I. Taylor, Proc. R. Soc. London Ser. A **201**, 192 (1950)
29. M. Fermigier, L. Limat, J.E. Wesfreid, P. Boudinet, C. Quillet, J. Fluid Mech. **236**, 349 (1992)
30. G.M. Carlomagno, in *Proceedings of the Second AIMETA Congress* (1974), p. 253
31. W.G. Pritchard, J. Fluid Mech. **165**, 433 (1986)
32. F. Giorgiutti, A. Bleton, L. Limat, J.E. Wesfreid, Phys. Rev. Lett. **74**, 538 (1995)
33. F. Giorgiutti, L. Limat, Physica D **103**, 590 (1997)
34. F. Giorgiutti, L. Limat, J.E. Wesfreid, Phys. Rev. E **57**, 2843 (1998)
35. P. Coullet, G. Iooss, Phys. Rev. Lett. **64**, 866 (1990)
36. R.E. Goldstein, G.H. Gunaratne, L. Gil, P. Coullet, Phys. Rev. A **43**, 6700 (1991)
37. S. Fauve, S. Douady, O. Thual, J. Phys. II France **1**, 311 (1991)
38. B. Caroli, C. Caroli, S. Fauve, J. Phys. I France **2**, 281 (1992)
39. H. Riecke, H.G. Paap, Phys. Rev. A **45**, 8605 (1992)
40. L. Gil, Europhys. Lett. **48**, 156 (1999)
41. L. Gil, Physica D **147**, 300 (2000)
42. F. Daviaud, M. Bonetti, M. Dubois, Phys. Rev. A **42**, 3388 (1990)
43. I. Mutabazi, C.D. Andereck, Phys. Rev. Lett. **70**, 1429 (1993)
44. P. Brunet, G. Gauthier, L. Limat, D. Vallet, Exp. Fluids **37**, 645 (2004)
45. C. Pirat, C. Mathis, P. Maissa, L. Gil, Phys. Rev. Lett. **92**, 104501 (2004)
46. C. Pirat, A. Naso, J.-L. Meunier, P. Maissa, C. Mathis, Phys. Rev. Lett. **94** 134502 (2005)
47. I. Aranson, L. Kramer, Rev. Mod. Phys., **74** 99 (2002)
48. P. Brunet, Ph.D. Thesis, Paris 6 University (2002), available online at: `http://tel.ccsd.cnrs.fr/documents/archives0/00/00/22/42/index_fr.html`
49. E.M. Nicola, M. Or-Guil, W. Wolf, M. Bar, Phys. Rev. E **65** 055101(R) (2002)
50. M. Howard, M. van Hecke, Phys. Rev. E **68** 026213 (2003)
51. R. Mikkelsen, M. van Hecke, T. Bohr, Phys. Rev. E **67** 046207 (2003)
52. P. Brunet, C. Clanet, L. Limat, Phys. Fluids **16** 2688 (2004)
53. V.G. Levich, *Physicochemical Hydrodynamics* (Prentice Hall, 1962)
54. B.A. Malomed, M.I. Tribelsky, Physica D **14** 67 (1984)
55. M.R.E. Proctor, C.A. Jones, J. Fluid Mech. **188** 301 (1988)
56. H. Levine, W.J. Rappel, H. Riecke, Phys. Rev. A **43** 1122 (1991)
57. F. Giorgiutti, Ph.D. thesis, Paris 6 University (1995)
58. P. Brunet, Phys. Rev. E (2006), submitted